POLITECNICO DI TORINO
Repository ISTITUZIONALE

Bixbyite-structured high-entropy oxide (CeZrYbErGd)O+ for visible-light photocatalytic degradation of gallic acid: Performance and energy efficiency

Original
Bixbyite-structured high-entropy oxide (CeZrYbErGd)O+ for visible-light photocatalytic degradation of gallic acid: Performance and energy efficiency / Mancuso, A., Monzillo, K., Sacco, O., Spiridigliozzi, L., Monfreda, V., Muscatello, A., Dell'Agli, G., Esposito, S., Vaiano, V.. - In: CATALYSIS TODAY. - ISSN 0920-5861. - 473:(2026), pp. 1-17. [10.1016/j.cattod.2026.115824]

Availability:
This version is available at: 11583/3017222 since: 2026-10-29T21:47:13Z

Publisher:
Elsevier

Published
DOI:10.1016/j.cattod.2026.115824

Terms of use:

This article is made available under terms and conditions as specified in the corresponding bibliographic description in the repository

Publisher copyright

(Article begins on next page)

07 November 2026

Catalysis Today 473 (2026) 115824

Contents lists available at ScienceDirect

Catalysis Today

journal homepage: www.elsevier.com/locate/cattod

Bixbyite-structured high-entropy oxide $(CeZrYbErGd)_2O_{3+\delta}$ for visible-light photocatalytic degradation of gallic acid: Performance and energy efficiency

Antonietta Mancuso [a,*], Katia Monzillo [a], Olga Sacco [b], Luca Spiridigliozzi [c,*], Viviana Monfreda [c], Andrea Muscatello [d], Gianfranco Dell'agli [c,e], Serena Esposito [d], Vincenzo Vaiano [a]

[a] Department of Industrial Engineering, University of SalernoVia Giovanni Paolo II 132, Fisciano, SA 84084, Italy
[b] Department of Chemistry and Biology "A.Zambelli", University of Salerno, Via Giovanni Paolo II 132, Fisciano, SA 84084, Italy
[c] Department of Civil and Mechanical Engineering, University of Cassino and Southern Lazio, Via G. Di Biasio 43, Cassino, FR 03043, Italy
[d] Department of Applied Science and Technology – INSTM Torino-Politecnico, Corso Duca degli Abruzzi, Torino 24 - I-10129, Italy
[e] INSTM—National Interuniversity Consortium of Materials Science and Technology, Florence 50121, Italy

ARTICLE INFO

Keywords:
Bixbyite-structured High Entropy Oxide
Heterogeneous photocatalysis
Visible light
Gallic acid

ABSTRACT

This work reports the synthesis of a bixbyite-structured High Entropy Oxide $(Ce_{0.2}Zr_{0.2}Yb_{0.2}Er_{0.2}Gd_{0.2})_2O_{3+\delta}$ via a co-precipitation route in an ammonia-based medium and its application as a visible-light-active photocatalyst for the degradation of gallic acid (GA), a model phenolic contaminant. Structural characterization demonstrated that calcination at 750 °C (CZYbEG-750) produced a nanocrystalline bixbyite-structured high-entropy oxide with lower crystallite size and defect-related vibrational features, while calcination at 1500 °C led to a well-crystallized system with bigger crystallites and very low surface area, detrimental to photocatalytic activity. Under optimal conditions (0.125 g L^{-1} catalyst, 5 mg L^{-1} GA initial concentration, pH 4.5), CZYbEG-750 achieved nearly complete GA removal (~99%) and 72% mineralization after 180 min of visible light irradiation. The photocatalytic performance was strongly affected by solution pH, with spontaneous acidic conditions (pH 4.5) yielding the highest degradation efficiency. Response surface methodology (RSM) and ANOVA identified irradiation time and pH as the most significant factors influencing performance ($R^2 = 0.9905$). Mechanistic investigation based on reactive oxygen species (ROS) scavenger tests and band edge calculations identified photogenerated holes as the main oxidative species, with hydroxyl and superoxide radicals contributing synergistically to the degradation process. The catalyst showed good stability, maintaining activity over five reuse cycles with minimal loss of efficiency, and retained ~85% degradation efficiency in tap water despite the presence of inhibitory inorganic ions. Compared to other photocatalytic systems, CZYbEG-750 exhibited competitive kinetics and remarkably low electrical energy consumption (~40 kWh m^{-3}), underscoring its energy efficiency. These findings highlight the potential of entropy-stabilized bixbyite-type high entropy oxides as robust and durable photocatalysts for the removal of recalcitrant, non-chromophoric pollutants in advanced water treatment applications.

1. Introduction

The health and stability of aquatic ecosystems are increasingly threatened by the contamination of natural water bodies with persistent organic pollutants (POPs), which are continuously released from industrial, agricultural, and domestic activities [1–4]. Among these, phenolic compounds represent a particularly concerning class of contaminants due to their high chemical stability, notable toxicity even at low concentrations, and ubiquitous presence in wastewater from petrochemical, pharmaceutical, pulp and paper, and textile industries [5–7].

Gallic acid (GA) (Fig. 1), a naturally occurring trihydroxybenzoic acid, is a representative member of this group. It is widely employed in food, pharmaceutical, cosmetic, and leather tanning industries owing to

* Corresponding authors.
E-mail addresses: anmancuso@unisa.it (A. Mancuso), l.spiridigliozzi@unicas.it (L. Spiridigliozzi).

https://doi.org/10.1016/j.cattod.2026.115824
Received 19 October 2025; Received in revised form 16 April 2026; Accepted 22 April 2026
Available online 26 April 2026
0920-5861/© 2026 The Authors. Published by Elsevier B.V. This is an open access article under the CC BY license (http://creativecommons.org/licenses/by/4.0/).

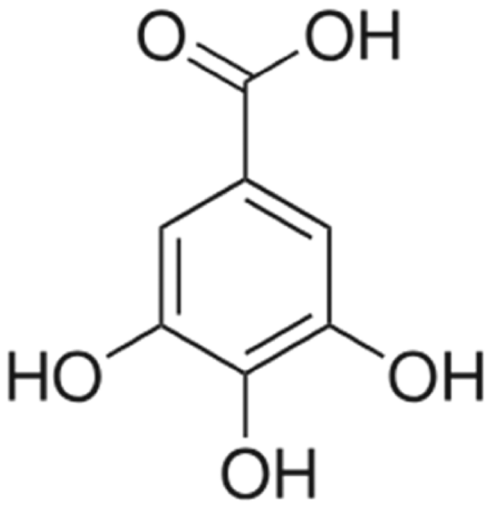


Fig. 1. GA molecular structure.

its antioxidant and antimicrobial properties [8,9]. Despite its natural origin, GA can persist in aquatic environments, particularly in wastewaters with elevated organic load and limited biodegradability, where its strong antioxidant character and aromatic structure hinder oxidative breakdown [10–12]. Its persistence may disrupt microbial balance, increase biological oxygen demand, and inhibit enzymatic activity, while its colorless nature complicates detection and timely remediation. Developing efficient, sustainable strategies for its removal is therefore a priority.

Heterogeneous photocatalysis has emerged as one of the most promising advanced oxidation processes (AOPs) for the degradation of persistent pollutants, as it exploits semiconductor activation under light irradiation to generate reactive oxygen species (ROS) [13–16]. While TiO_2 and ZnO have been extensively studied [17–20], their wide band gaps and fast charge recombination restrict efficiency under visible light [21–23].

To overcome these limitations, the main specific objective of the present study is the identification of a new photocatalyst able to degrade POP under visible light. To this end, high entropy oxides (HEOs) have emerged as a novel class of photocatalysts with tunable band structures, enhanced defect chemistry, and remarkable structural stability [24–27]. Their multicomponent nature promotes oxygen vacancy formation, broad light absorption, and improved charge carrier dynamics, making them particularly suited for visible-light photocatalysis [28]. Although HEOs have shown promising activity in dye and pharmaceutical degradation [29–32], little is known about their performance against non-chromophoric and oxidation-resistant pollutants such as GA, which pose greater challenges for photocatalysis.

Based on our previous findings [33], in which a bixbyite-structured HEO $(Ce_{0.2}Zr_{0.2}Yb_{0.2}Er_{0.2}Gd_{0.2})_2O_{3+\delta}$ showed very good catalytic activity toward dye degradation, we decided to use the same HEO also for the POP degradation. To the best of our knowledge, this is the first comprehensive study demonstrating the application of a bixbyite-structured HEO for the photocatalytic removal of GA under visible light.

Hence, we report the synthesis of a bixbyite-structured HEO, $(Ce_{0.2}Zr_{0.2}Yb_{0.2}Er_{0.2}Gd_{0.2})_2O_{3+\delta}$, via a simple co-precipitation method using ammonia as the precipitating agent. GA was selected as a target pollutant not only because of its widespread industrial use and environmental occurrence [8], but also as a representative model compound of the polyphenol family frequently employed in photocatalytic studies [34,35]. Its non-chromophoric structure excludes photosensitization effects, while its strong antioxidant character makes it a more challenging substrate for visible-light photocatalysis compared to conventional dye pollutants.

In the present study, the material was systematically evaluated for the photocatalytic degradation of GA under visible light, with particular attention to operational parameter optimization, energy efficiency assessment, and identification of the main reactive oxygen species involved in the process. The aim of this work is not to elucidate a detailed degradation pathway, but rather to evaluate the visible-light photocatalytic performance of the material and identify the predominant reactive species involved in GA degradation. This study may contribute to the growing field of high entropy oxide photocatalysts by establishing a systematic correlation between structural features, defect chemistry, optical properties, and photocatalytic activity toward a non-chromophoric phenolic pollutant, together with an assessment of energy efficiency and performance in a realistic water matrix.

2. Materials and methods

2.1. Chemicals

$ZrO(NO_3)_2$ (99.9%, Carlo Erba, Milan, Italy), $Ce(NO_3)_3 \bullet 6\,H_2O$, $Yb(NO_3)_3 \bullet 5\,H_2O$, $Gd(NO_3)_3 \bullet 6\,H_2O$, and $Er(NO_3)_3 \bullet 5\,H_2O$ (99.9%, Sigma Aldrich, Milan, Italy) were employed as metal precursors, while an ammonia solution (NH_3 solution 30%, Carlo Erba, Italy) served as the precipitating agent for the synthesis of CZYbEG. GA ($C_7H_6O_5$, powder, 98%, Thermo Scientific), hydrochloric acid (HCl, 37%, Carlo Erba, Milan, Italy), and sodium hydroxide (NaOH, pellets anhydrous, $\geq$ 98%, Sigma Aldrich, Milan, Italy) were used for the photocatalytic tests. All reagents were used as-purchased without further purification.

2.2. Synthesis of HEO photocatalyst

The adopted synthesis procedure for $(Ce_{0.2}Zr_{0.2}Yb_{0.2}Er_{0.2}Gd_{0.2})_2O_{3+\delta}$ (CZYbEG) was as follows: (i) all rare-earth nitrates and zirconyl nitrate were dissolved in deionized water to obtain a total cation concentration of 0.1 M (with each cation at 0.02 M), yielding solution A, which was vigorously stirred to ensure complete dissolution; (ii) in parallel, the precipitating solution B was prepared to reach a nominal ammonia concentration of 2 M upon coprecipitation; (iii) solution B was then rapidly added to solution A under mild stirring, leading to the immediate formation of a pinkish precipitate; (iv) the resulting suspension was filtered under vacuum, thoroughly washed with deionized water, and dried overnight at 80 °C in static air.

The as-prepared CZYbEG powder underwent two different calcination treatments, i.e., at 750 °C and 1500 °C, respectively, to promote the entropy-driven stabilization of the designed bixbyite-like phase according to the so-called standard deviation predictor for rare-earth-based HEOs [36,37].

Given that no optimization of the calcination temperature was carried out, the rationale behind the chosen conditions is reported in the following. to select a very low temperature—still capable of yielding a single phase (750 °C, in agreement with the authors' previous studies)—and then a very high temperature (1500 °C) to assess possible metastability phenomena of the low-temperature–synthesized bixbyite HEO.

2.3. Photocatalyst characterization

Structural characterization of the as-prepared and calcined CZYbEG powders was conducted via X-ray diffraction (XRD) using a Panalytical X'PERT MPD diffractometer with Cu Kα radiation.

Thermal analysis (TG/DTA) of the as-precipitated powder was performed in air at a heating rate of 10 °C min^{-1}, using α-Al_2O_3 as a reference material, with a Netzsch Thermoanalyzer STA 409.

The specific surface area of both the as-precipitated and calcined powders was measured by nitrogen adsorption/desorption (Gemini, Micromeritics) following drying at 400 °C and was evaluated using the Brunauer–Emmett–Teller (BET) method.

CZYbEG morphology and chemical composition were inspected via

Scanning Electron Microscopy (SEM) by using a Philips microscope (XL30) coupled with an electron-dispersive spectroscopy (EDS) probe.

An integrated confocal micro-Raman system (Invia Micro-Raman, Renishaw, Wotton-under-Edge, UK) was used to acquire the CZYbEG Raman spectra. Notch filters are used in the spectrometer to filter out the Rayleigh excitation line. Radiation at 514 nm was used for measurements, with an actual output power of 25 mW. At a magnitude of 20 ×, the spectra were obtained on the focalized sample.

Optical characterization was carried out using a Varian Cary 5000 UV-Vis spectrophotometer equipped with a diffuse reflectance (DR) integrating sphere, operating in the 200–900 nm range. The absorption spectra were processed using the Kubelka–Munk function, F(R). The optical band gap (Eg) was estimated using the Tauc approach, based on the relation $(F(R)h\nu)^{\gamma} = f(h\nu)$, where γ is 2 for direct transitions and 1/2 for indirect transitions.

The ζ-potential was determined by measuring the electrophoretic mobility at 25 °C as a function of pH using dynamic light scattering (DLS) with a Zetasizer Nano ZS90 (Malvern Instruments, Worcestershire, UK). pH measurements were performed using an XS pH70 Viop meter (GEASS, Turin, Italy). A 1 mM $CaCl_2$ solution was prepared with ultrapure Milli-Q water, and 0.5 g of the HEO sample was dispersed in 100 mL of this solution. The suspension was sonicated for 15 min (10 W/mL, 20 kHz) using a DU-65 sonicator (Argo Lab, Carpi, Italy). The pH was adjusted by the addition of 0.1 M NaOH for alkaline conditions or 0.1 M HCl for acidic conditions.

2.4. Photocatalytic activity test

Photocatalytic tests were carried out in a cylindrical Pyrex photoreactor (ID = 2.6 cm, L = 41 cm, V = 100 mL) equipped with an air distributor (142 Ncc min^{-1}). Irradiation was provided by a visible LED strip (nominal power: 10 W; emission range: 400–800 nm; irradiance: 13 mW cm^{-2}) placed in direct contact with the external wall of the reactor to ensure homogeneous exposure. Catalyst powders (0.06–0.25 g L^{-1}) were suspended in 100 mL of aqueous gallic acid (GA) solutions (initial concentrations: 5, 7.5, 10 mg L^{-1}) at spontaneous pH. Suspensions were kept in the dark for 120 min to allow adsorption–desorption equilibrium. The influence of pH was evaluated by adjusting the natural value (≈4.5) with hydrochloric acid (HCl, Carlo Erba) or sodium hydroxide (NaOH, Sigma-Aldrich) solutions. Reaction progress was monitored by periodically withdrawing 2 mL aliquots, which were analyzed with a UV–Vis spectrophotometer (Thermo Scientific Evolution 201) at 270 nm to follow GA degradation [34].

To validate the spectrophotometric determination of gallic acid (GA), additional analyses were performed by high-performance liquid chromatography (HPLC). The measurements were carried out using a Dionex UltiMate 3000 (Thermo Scientific) system equipped with a diode array detector (DAD), column thermostat, and automatic injector with a 100 μL loop. Chromatographic separation was achieved using a Phenomenex Luna C-18 column (150 × 4.6 mm i.d.; 5 μm particle size), maintained at 35 °C. The mobile phase consisted of water acidified with 0.1% formic acid (solvent A) and acetonitrile (solvent B), using the following gradient program: 0–14 min, 15% B (isocratic); 14–23 min, 60–100% B (linear gradient); 23–30 min, 15% B (isocratic). The flow rate was set at 0.8 mL min^{-1}, the injection volume was 50 μL, and detection was performed at 270 nm.

Mineralization was determined from total organic carbon (TOC) removal, measured as CO_2 produced by catalytic oxidation at 680 °C [38].

The kinetics of GA degradation were evaluated using the Langmuir–Hinshelwood model, which describes the photocatalytic rate (r) as:

$$r = \frac{dC}{dt} = -\frac{k_r \times K_{ad} \times C}{1 + K_{ad} \times C} \quad (1)$$

Where k_r, K_{ad}, and C represent the intrinsic kinetic constant, adsorption equilibrium constant, and contaminant concentration, respectively.

At the low pollutant concentrations investigated, Eq. (1) can be simplified to a pseudo-first-order expression:

$$-\ln\left(\frac{C}{C_0}\right) = k_r \times K_{ad} \times t = k_{app} \times t \quad (2)$$

The slope of -ln (C/C_0) vs. time plot provides the apparent kinetic constant (k_{app}).

Degradation and mineralization efficiencies were calculated as:

$$Degradation\ efficiency(t) = \left(1 - \frac{C(t)}{C_0}\right) \times 100 \quad (3)$$

$$Mineralization\ efficiency(t) = \left(1 - \frac{TOC(t)}{TOC_0}\right) \times 100 \quad (4)$$

Where $TOC(t)$ is the total organic carbon at the generic irradiation time (mg L^{-1}), TOC_0 is the initial total organic carbon (mg L^{-1}), $C(t)$ is the GA concentration at the generic irradiation time (mg L^{-1}), and C_0 is the initial GA concentration (mg L^{-1}).

2.5. Box-behnken design

To evaluate the influence of operating variables on GA degradation and to identify optimal conditions, a Box–Behnken design (BBD) was applied using RStudio software (v. 4.5.1, 2025–06–13 ucrt). This response surface methodology enables the systematic assessment of three or more variables with a reduced number of experiments, while preserving statistical robustness [39]. Each factor was investigated at three coded levels (−1, 0, +1), as summarized in Table 1.

This design allows the estimation of linear, interaction, and quadratic effects, supporting the development of predictive models and the identification of optimal operating conditions. Three independent variables were considered: irradiation time (X_1, min), catalyst loading (X_2, g L^{-1}), and solution pH (X_3, dimensionless). A total of 15 experimental runs were performed according to the Box–Behnken design. The relationship between the response variable and the experimental factors was described by a second-order polynomial regression model, expressed as:

$$R = \beta_0 + \sum_{i=1}^{k} \beta_i \times x_i + \sum_{i=1}^{k} \beta_{ii} \times x_i^2 + \sum_{i=1}^{k-1} \sum_{j=i+1}^{k} \beta_{ij} \times x_i \times x_j + \varepsilon$$

Where:

R= response variable (e.g C/C_0);

X_i and X_j= coded independent variables;

β_0= intercept;

β_i β_{ii} and β_{ij}= coefficients for linear, quadratic and interaction terms, respectively;

k = number of independent variables.

The sign of each coefficient indicates the nature of the effect: positive values correspond to synergistic contributions that enhance GA degradation, whereas negative values denote antagonistic effects that limit the response. Optimal conditions were determined by analyzing the fitted regression model together with the response surface and contour plots.

Table 1
Experimental ranges and levels of independent factors.

Factors design	Factors	Ranges and levels		
		-1	0	+ 1
X1	Time	0	30	60
X2	Catalyst dosage	0.06	0.125	0.25
X3	pH	2	4.5	7

3. Results and discussion

3.1. Structural characterization

Fig. 2 shows the diffraction pattern of both the as-precipitated CZYbEG sample (i.e., CZYbEGTQ) and the differently calcined systems (i.e., CZYbEG-750 and CZYbEG-1500). The choice of both calcination temperatures was dictated by the thermogravimetric analysis (discussed in the following) carried out on the as-precipitated system.

Confirming previous results [40], the as-precipitated sample is fully amorphous, with notably broad halos ascribable to the typical short-range order of amorphous ceria/zirconia-based precipitates.

On the other hand, after calcination at 750 °C, a nanocrystalline material is formed, as evidenced by the very broad diffraction peaks. Owing to its nanocrystalline nature and to the strong similarity between the diffraction patterns of fluorite and bixbyite, the actual crystalline phase of the samples calcined at 750 °C cannot be unambiguously identified from Fig. 2a. However, total scattering measurements [40] of CZYbEG-750 performed at beamline ID31 at the European Synchrotron Radiation Facility (ESRF) (see Figure S1) allowed this ambiguity to be resolved: the material adopts the bixbyite structure, and several weak reflections characteristic of this phase are actually present in Figure S1, and they are labeled with "*".Details of the experimental procedure, along with the measurement results (Figure S1), are reported in the Supplementary Materials.

Finally, upon calcination at 1500 °C, CZYbEG-1500 is indeed an entropy-stabilized bixbyite-like phase (ICDD card n. 00–012–0797), as clearly evident by the presence of the weak reflections (belonging to the bixbyite-like crystal structure), some of them labeled with "*" in Fig. 2.

The crystallite size (nm) in both calcined systems was calculated from the (222) reflection of the bixbyite phase at 2θ of about 29.1 ° using the Scherrer equation, resulting in around 5 nm and 150 nm for CZYbEG-750 and CZYbEG-1500, respectively.

3.2. Thermal behavior

To analyze in detail the CZYbEG-TQ thermal behavior prior to the entropy-driven formation of the bixbyite-like phase, a simultaneous differential thermal analysis (DTA) and thermogravimetric analysis (TG) has been carried out on it.

Fig. 3 shows the DTA-TG curves of CZYbEG-TQ, revealing a rather interesting thermal behavior with four different endothermic thermal events (α, β, γ and δ) located at about 180, 220, 480 and 1300 °C, respectively. Particularly, the first three thermal events, i.e., α, β and γ are attributable to parallel decomposition of different as-precipitated rare-earth hydroxides/hydrated oxides [41] and zirconium hydroxide [42]. Interestingly, the high-temperature δ event, occurring at about 1300 °C, could be attributed to the full entropy-driven stabilization of the designed bixbyite-like single phase, being associated with a small weight loss due to a minor oxygen evolution very likely driven by the full Ce^{+4} to Ce^{+3} reduction. This evidence suggests that structure of CZYbEG-750 sample is indeed a metastable bixbyite.

3.3. BET analysis

The specific surface area of both the calcined CZYbEG systems, i.e., CZYbEG-750 and CZYbEG-1500, was measured by nitrogen adsorption analysis according to the BET (Brunauer–Emmett–Teller) method. However, due to the very low surface area values measured for both systems, only an upper limit estimation has been reported in the following Table 2.

Anyway, a direct correlation between the decrease in surface area and the increasing calcination temperature is still observed, with both CZYbEG-750 and CZYbEG-1500 exhibiting very low surface areas compared to similar systems co-precipitated in a carbonate environment [33].

3.4. SEM analysis

Fig. 4 presents representative SEM micrographs of CZYbEG-750 (Fig. 4a) and CZYbEG-1500 (Fig. 4b). Both samples exhibit similar morphologies, albeit at different length scales (due to the different calcination temperatures adopted). In each case, the powders consist of large, irregular agglomerates(exceeding 100 μm in the CZYbEG-1500 system) composed of smaller primary particles, a behavior typical of rare-earth–based systems precipitated using ammonia [41].

Additionally, to further assess the homogeneous distribution of the different cations present within the two CZYbEG systems, an EDS elemental mapping has been carried out on both CZYbEG-750 and CZYbEG-1500, and it is reported within the Supplementary Materials (Figure S2 and Figure S3). Such EDS elemental maps, for both the samples, reveal a homogeneous spatial distribution of the constituent cations (Ce, Zr, Yb, Er, and Gd) as well as oxygen. This uniformity confirms the effectiveness of the adopted synthesis protocol and supports the formation of a single-phase bixbyite-type high-entropy oxide. The absence of detectable compositional segregation or clustering further indicates that all elements are well distributed into the crystal lattice, consistent with the expected configurational stabilization of the multicomponent oxide, even upon calcination at 750 °C.

3.5. Raman analysis

The Raman spectrum of CZYbEG-750 (Figure S4) displays a main band in the 400–500 cm^{-1} region, consistent with the F_2g mode of oxygen vibrations in the ceria sublattice [43−45]. Additional features near 500 and 615 cm^{-1} are associated with lattice disorder and oxygen vacancies, originating from the interaction of multiple dopant cations with the ceria matrix [46,47]. A weaker high-frequency contribution in the 800–1000 cm^{-1} range further confirms the presence of a highly disordered fluorite-like structure [48,49].

3.6. UV-Vis characterization

The optical properties of the CZYbEG-750 sample were investigated using UV-Vis diffuse reflectance spectroscopy. The absorption spectrum, shown in Figure S5, was analyzed through the Tauc method to estimate the optical band gap. As illustrated in Fig. 5, the plots of $(F(R)(h\nu)^{\gamma}$ versus $h\nu$ were constructed for both direct ($\gamma = 2$) and indirect ($\gamma = 1/2$) transitions. The extrapolation of the linear regions yielded band gap values of 3.3 eV (direct) and 2.8 eV (indirect), respectively.

These lower Eg values, compared to those previously obtained for the same composition synthesized via carbonate precipitation (3.7 eV direct, 3.2 eV indirect) [33], highlight the critical role of synthesis conditions in tuning the optical properties of HEOs

The lower Eg values obtained in this study reflect a redshift in the absorption edge, potentially enhancing visible light absorption. Moreover, narrow and well-defined absorption features are observed in the 400–700 nm range, as shown in Figure S5 of the Supplementary Material. These are attributed to intra-4f electronic transitions of rare-earth ions such as Er^{3+}, Yb^{3+}, and Gd^{3+} [33]. Similar to previous studies on rare-earth-containing oxides, these f–f transitions may introduce localized electronic states within the band structure, which can facilitate stepwise excitation processes and extend light absorption into the visible region [50]. In addition to these discrete transitions, the visible-light response of multicomponent ceria-based systems is frequently associated with the presence of oxygen vacancies and disorder-induced sub--band-gap states. Such defect-related electronic states generate an absorption tail beyond the fundamental band edge and promote charge carrier activation under visible irradiation [51].

In HEOs, the intrinsic compositional disorder and lattice distortion further favor the formation of localized electronic states and band tailing effects, which may effectively narrow the optical absorption threshold and enhance visible-light utilization [52,53]. Therefore, besides the

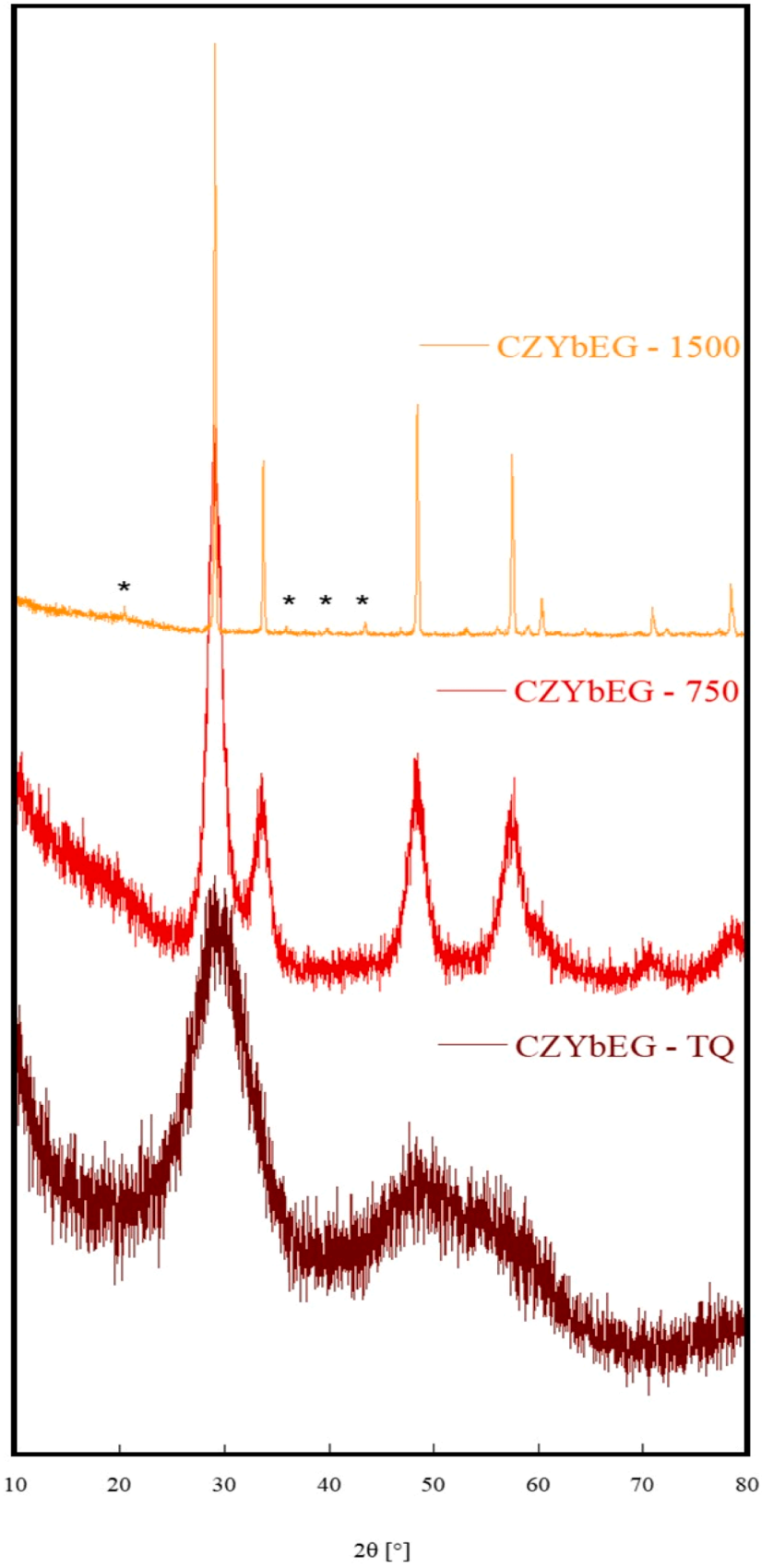


Fig. 2. Diffraction patterns of both as-precipitated (CZYbEG-TQ) and calcined at either 750 °C (CZYbEG-750) and 1500 °C (CZYbEG-1500) CZYbEG system.

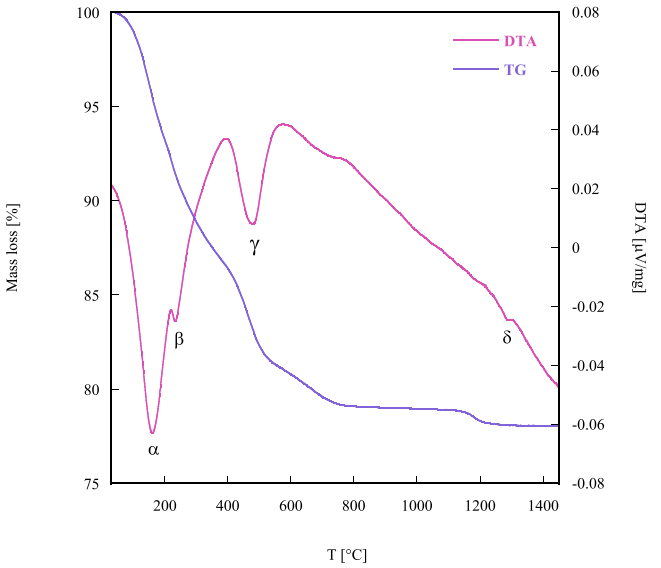


Fig. 3. DTA-TG curves of the as-precipitated CZYbEG system (CZYbEG-TQ).

Table 2
Specific surface areas and mean particle diameter of the as-prepared samples.

Sample labelling	Specific surface area [m^2/g]
CZYbEG-750	< 5.0
CZYbEG-1500	< 1.0

estimated direct (3.3 eV) and indirect optical band gap (2.8 eV), the combined contribution of intra-4f transitions and defect-related states can explain the efficient photocatalytic activity of CZYbEG-750 under visible irradiation (*vide infra*).

4. Photocatalytic activity results

4.1. Effect of calcination temperature

Fig. 6 shows the screening tests of CZYbEG photocatalysts calcined at 750 and 1500 °C. Photocatalytic performance was evaluated in terms of GA degradation and mineralization using 0.125 g L^{-1} of catalyst in a 10 mg L^{-1} GA solution (pH 4.5). Results were compared with photolysis experiments carried out under visible light in the absence of the catalyst.

The negligible GA and TOC removal observed under visible light in the absence of a catalyst confirms that photolysis does not contribute significantly to degradation. In contrast, CZYbEG-750 achieved the best performance, with 66% GA degradation and 62% mineralization after 180 min (Fig. 6). XRD analysis evidenced that the 750 °C treatment preserves the bixbyite single-phase structure with broadened reflections indicative of nanocrystallinity, whereas calcination at 1500 °C leads to sharper peaks as a consequence of the remarkable grain growth.

To further validate the reliability of the UV–Vis monitoring at 270 nm, the concentration of GA during photocatalytic tests was also determined by HPLC under the same experimental conditions. The chromatographic analysis confirmed the progressive decrease of GA. The concentrations obtained by HPLC were in very good agreement with those determined spectrophotometrically, with deviations within approximately 2%, thus confirming the accuracy of the UV–Vis method.

4.2. Influence of photocatalyst dosage

The effect of catalyst dosage on photocatalytic activity was evaluated for CZYbEG-750 using loadings between 0.06 and 0.25 g L^{-1} in 10 mg L^{-1} GA solution at natural pH (≈4.5) (Fig. 7). As shown in Fig. 7a, GA

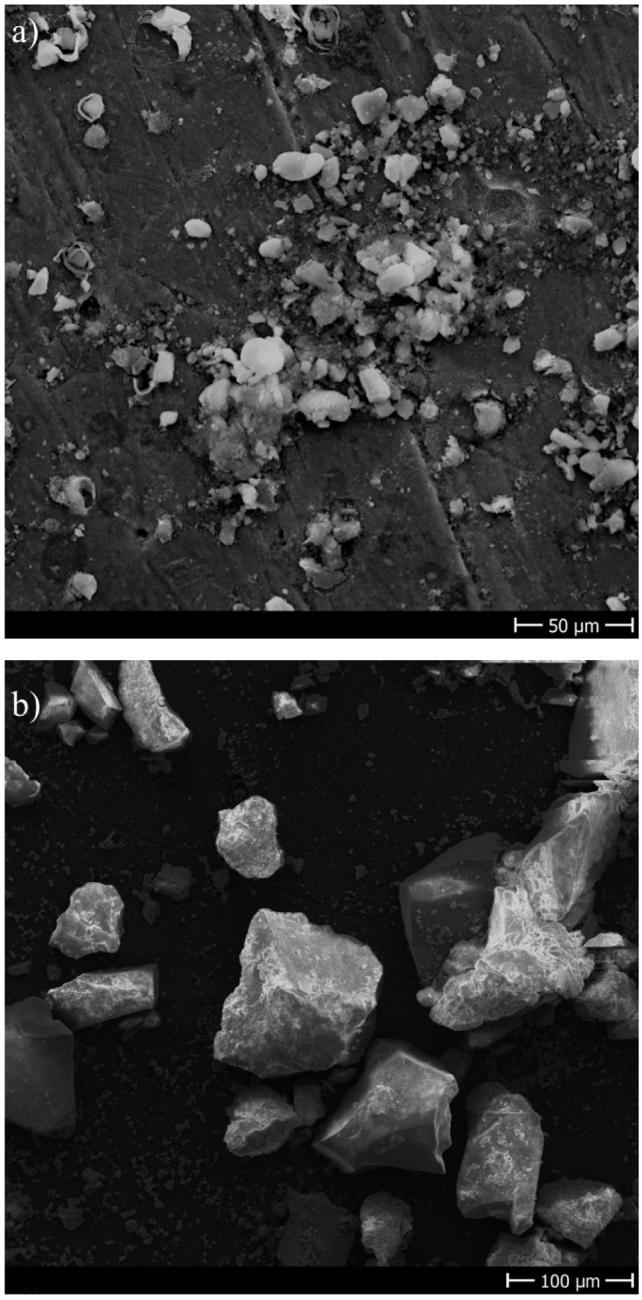


Fig. 4. Exemplary SEM micrographs of the calcined CZYbEG systems, either at 750 °C (CZYbEG-750) or at 1500 °C (CZYbEG-1500).

degradation increased with catalyst concentration under visible light irradiation, although the extent of improvement varied with time.

Before visible light irradiation, nearly all the GA (approximately 99%) was adsorbed onto the photocatalyst surface at dosages of 0.5 and 0.25 L^{-1}. Consequently, the photocatalytic degradation of GA could not be clearly observed during the irradiation period.

The significant adsorption observed can be attributed to the strong electrostatic interactions between the surface of CZYbEG-750 and the GA species. At the spontaneous pH of 4.5, GA is partially deprotonated [54]. This deprotonated form enhances the electrostatic attraction between the catalyst surface and the anionic GA, promoting efficient adsorption. Such interactions are crucial for optimizing the photocatalytic degradation process, as they facilitate a higher degree of pollutant-catalyst surface contact [34,53,55].

However, when the catalyst dosage was reduced to 0.125 L^{-1}, GA

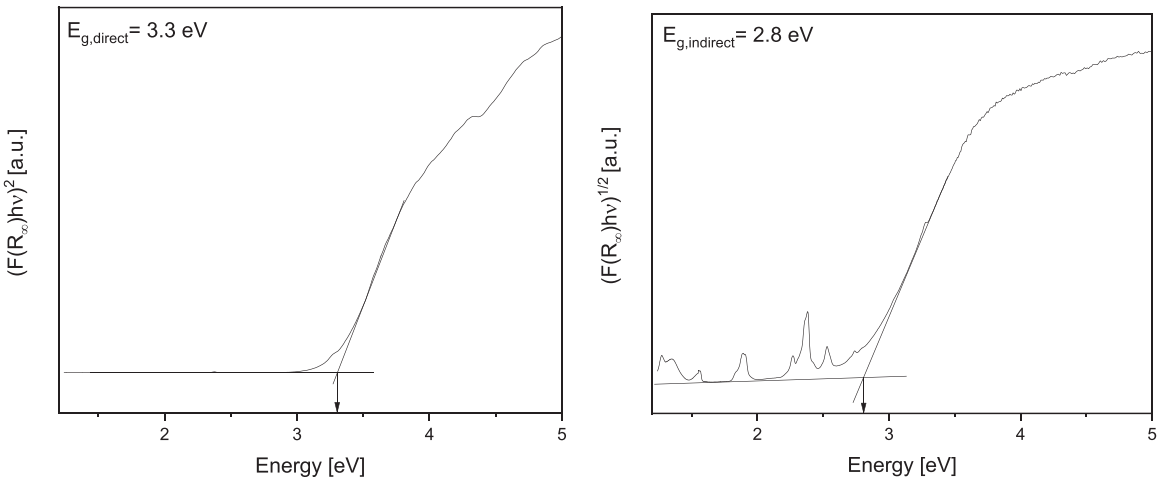


Fig. 5. Tauc plot for (a) direct bandgap calculation and (b) indirect bandgap calculation of the CZYbEG-750 sample based on the $F(R_\infty)$ function by Tauc plot relation using the double tangent approximation.

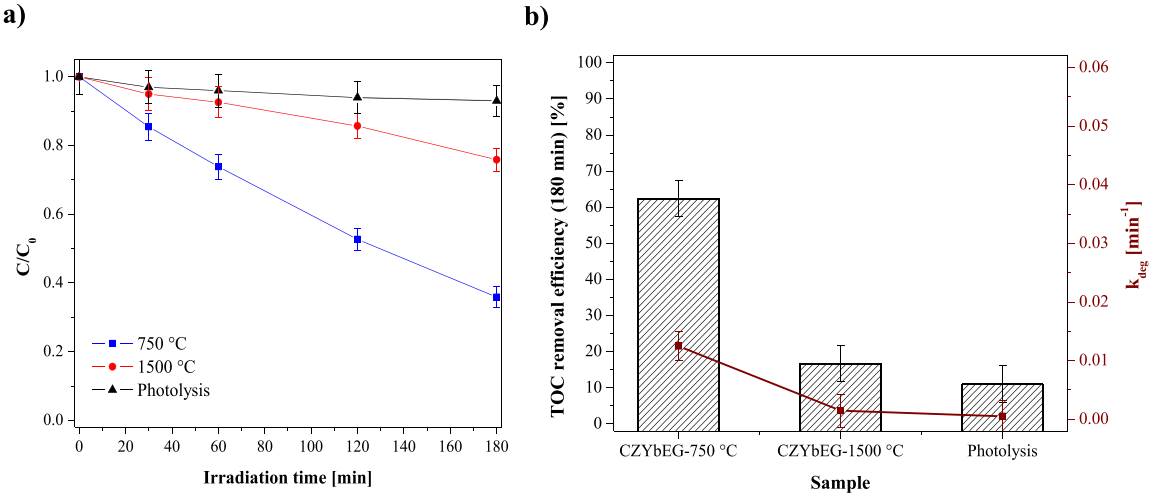


Fig. 6. a) GA relative concentration as a function of irradiation time; b) TOC removal efficiency (%) after 180 min of visible light achieved in the presence of CZYbEG samples and during the photolysis test.

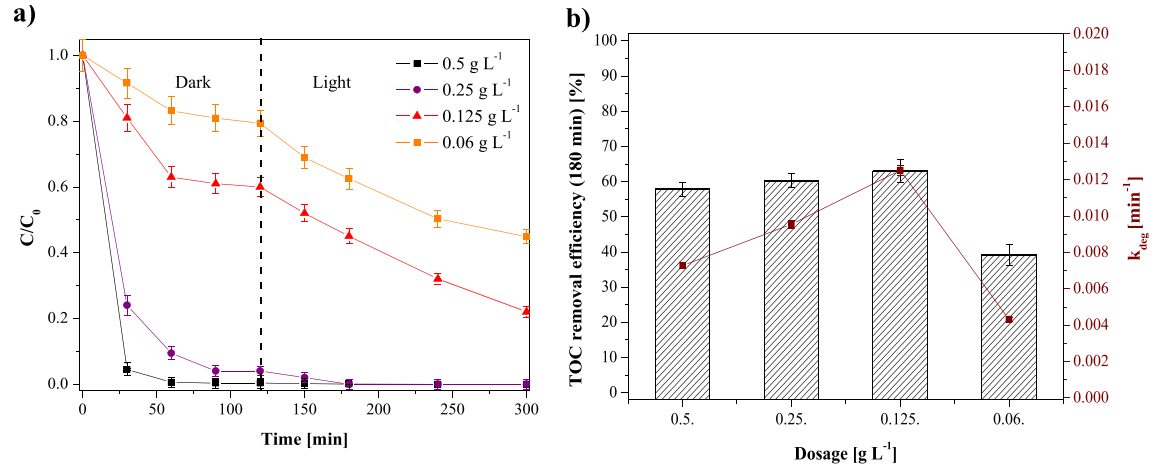


Fig. 7. a) GA relative concentration as a function of test time; b) TOC removal efficiency (%) after 180 min of visible light obtained with CZYbEG-750 at different dosages.

adsorption significantly decreased (~**40%** reduction), allowing the photocatalytic degradation process to become detectable. Under visible

light irradiation, the relative concentration of pollutant gradually declined, reaching a GA degradation efficiency of 63% after 180 min (Fig. 7a). In addition, GA mineralization was assessed at dosages of 0.125 L^{-1}, revealing a total organic carbon (TOC) removal of over 60% and a degradation rate constant of 0.0125 min^{-1} (Fig. 7b).

To explore the effect of a lower catalyst dosage, we also evaluated GA degradation at 0.06 L^{-1}. As expected, the photocatalytic activity decreased by approximately 20% compared to 0.125 L^{-1} (Fig. 7a), due to the limited availability of active sites and reduced formation of reactive species [56,57].

Overall, these results indicate that 0.125 g L^{-1} represents the optimal loading, striking a balance between adsorption and photocatalytic activity. The identification of this optimum provides a sound basis for the subsequent investigation of other operational parameters, such as the effect of GA initial concentration and solution pH.

4.3. Influence of GA initial concentration

The influence of the pollutant initial concentration was subsequently evaluated using 0.125 g L^{-1} of CZYbEG-750 at natural pH. A series of tests was performed by varying the initial GA concentration from 5 to 10 mg L^{-1} , and the results are reported in Fig. 8.

As shown in Fig. 8a, the highest photocatalytic activity was observed at 5 mg L^{-1} , where the system achieved nearly complete pollutant degradation (99.9%) after 180 min of visible light exposure. This was accompanied by a TOC removal efficiency of 72.3% and an apparent kinetic constant of 0.0399 min^{-1} (Fig. 8b).

The enhanced performance at lower pollutant concentrations can be attributed to the higher availability of active sites on the catalyst surface, which promotes the generation of reactive oxygen species (ROS) and facilitates more efficient pollutant oxidation. At higher GA concentrations (7.5 and 10 mg L^{-1}), the degradation rate decreased, consistent with partial occupation of the catalyst surface by excess GA molecules, which limits ROS formation. Several studies have reported this trend: at low initial pollutant concentrations, the catalyst surface is less saturated and ROS formation is more efficient, whereas at higher concentrations, the degradation efficiency decreases due to the occupation of active sites and the consequent limitation in ROS generation [58–60]. In addition, higher concentrations can also hinder light penetration due to optical shielding effects, further reducing photocatalytic efficiency [61–63].

Nevertheless, even at 10 mg L^{-1} , the catalyst maintained significant activity, reaching more than 60% TOC removal after 180 min (Fig. 8b). This result underscores the robustness of the CZYbEG-750 photocatalyst and its suitability for the degradation of phenolic contaminants at different concentration levels. Similar concentration-dependent behaviors have also been reported for other high-entropy oxide systems [32], confirming that the observed trend is consistent with the Langmuir–Hinshelwood kinetic model, where pollutant loading plays a critical role in controlling degradation rates.

4.4. Influence of pH

The influence of pH on the photocatalytic performance of CZYbEG-750 was evaluated under optimal conditions (0.125 g L^{-1} catalyst dosage, 5 mg L^{-1} GA). The natural solution pH (≈4.5) was adjusted to 2, 7, or 12 with 0.1 M HCl or NaOH, and the results are shown in Fig. 9.

The highest GA adsorption occurred at spontaneous pH (4.5), with ~83% removal in the dark after 120 min (Fig. 9a). Under visible light, degradation was also maximized at pH 4.5, reaching ~99% after 180 min with an apparent rate constant of 0.0399 min^{-1} (Fig. 9b). A similar efficiency (98%) was observed at neutral pH, although mineralization was slightly lower (53% vs. 72.3%). In contrast, photocatalytic activity dropped drastically at pH 2 (41% degradation) and was almost suppressed at pH 12 (2.5%).

The zeta potential of CZYbEG-750 indicated a point of zero charge (PZC) near pH 8.3 (data not shown). Below this value, the surface is positively charged due to protonation of hydroxyl groups, whereas above it, deprotonation dominates, giving a negative charge [64]. In parallel, GA is mostly protonated at pH 2, progressively deprotonates between pH 4.5–7 to form anionic species, and is fully deprotonated under basic conditions [54,55].

Thus, at pH 4.5 and 7 (i.e., below PZC), electrostatic attraction between anionic GA species and the positively charged CZYbEG-750 surface enhances adsorption and promotes efficient ROS-mediated degradation. Conversely, at strongly acidic pH (2), the repulsion between protonated GA and the positively charged surface hinders adsorption, while at pH 12, both GA and the catalyst surface are negatively charged, resulting in almost complete loss of photocatalytic activity [17,53]. These findings highlight that pollutant adsorption, governed by electrostatic interactions, plays a pivotal role in determining photocatalytic performance.

4.5. Stability tests

To assess the stability and reusability of CZYbEG-750, five consecutive photocatalytic cycles were performed under the optimized conditions (0.125 g L^{-1} catalyst dosage, 5 mg L^{-1} GA initial concentration, pH 4.5). After each cycle, the catalyst was recovered by centrifugation, thoroughly rinsed with distilled water to remove adsorbed residues, and dried at 90 °C before reuse.

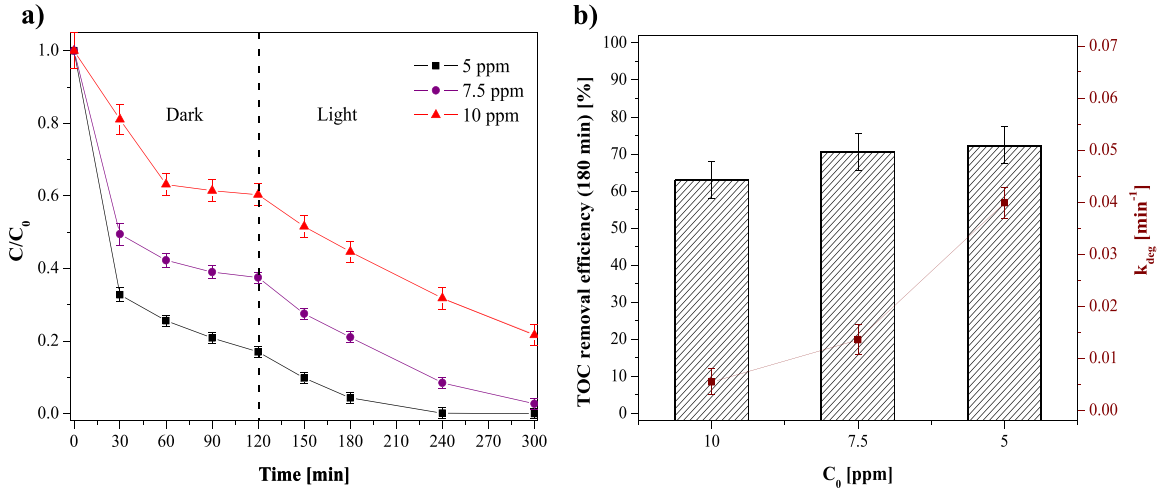


Fig. 8. a) GA relative concentration as a function of test time; b) TOC removal efficiency (%) after 180 min of visible light by varying the GA initial concentration.

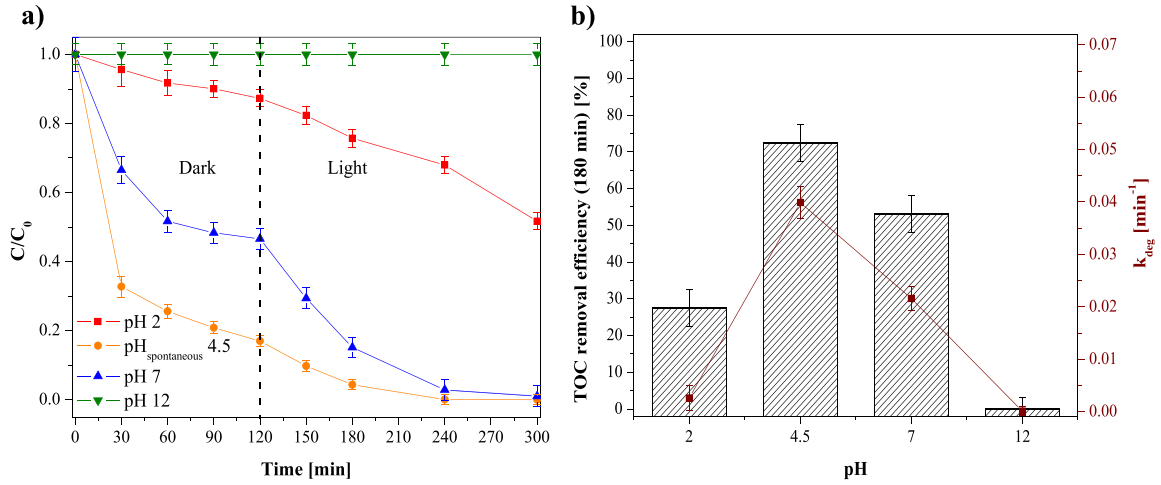


Fig. 9. a) GA relative concentration as a function of test time; b) TOC removal efficiency (%) after 180 min of visible light by varying the solution pH.

As shown in Fig. 10, GA degradation efficiency decreased from approximately 99.9% in the first cycle to about 80% after the fifth cycle, corresponding to ~80% retention of the initial activity. Similarly, mineralization efficiency (TOC removal) decreased from about 72% to approximately 62%, corresponding to ~86% retention after five reuse cycles. Although a moderate decline in performance was observed, the catalyst maintained a high fraction of its initial photocatalytic efficiency, indicating good operational stability.

To evaluate possible structural modifications after reuse, the recovered sample was characterized by Raman spectroscopy (Figure S6). The Raman spectra of the fresh and spent catalysts exhibit comparable vibrational features, with preservation of the characteristic bixbyite-related bands and no emergence of additional peaks attributable to secondary phases. No significant band shifts were detected, suggesting that the structural framework of CZYbEG-750 remains stable after repeated photocatalytic cycles. Compared with conventional oxide photocatalysts, which often suffer from more severe deactivation due to structural collapse or extensive surface poisoning [65,66], the present HEO system demonstrates remarkable durability under visible-light operation, consolidating its potential for practical wastewater treatment applications.

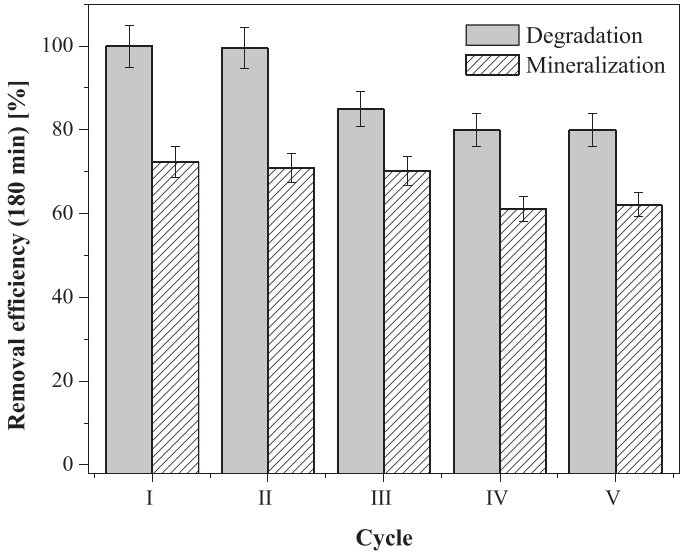


Fig. 10. GA degradation and mineralization after 180 min of visible light over five reuse cycles.

4.6. Construction of a polynomial expression and 3D response surface for AG photodegradation

The three-level matrix generated using the Box-Behnken design, along with the experimentally obtained responses for GA degradation efficiency (E), shown in Figures S7, S8, S9, and S10, is presented in Table 3.

Based on these results, two empirical quadratic models were developed to describe the relationships between the responses and the selected variables:

$$E(\%) = 1.4317 + 0.0013 \times X_1 - 1.4225 \times X_2 - 0.2145 \times X_3 + 0.0001 \times {X_1}^2 + 5.5150 \times {X_2}^2 + 0.0305 \times {X_3}^2 - 0.0039 \times X_1 \times X_2 - 0.0035 \times X_1 \times X_3 - 0.0530 \times X_2 \times X_3$$

The experimental responses versus the predicted ones are shown in Fig. 11; the predicted values approximate the observed values in all sets of experiments for C/C_0. The reliability of the quadratic model was confirmed by statistical parameters: the coefficient of determination ($R^2 = 0.9905$) and the adjusted R^2 (0.9735), both indicating an excellent fit. Such high correlation highlights the robustness of the model and its capability to predict GA degradation efficiency under different operational conditions.

Furthermore, the adequacy of the quadratic model was evaluated by analysis of variance (ANOVA), which assesses the statistical significance

Table 3
Box-Behnken design with experimental values for independent variables: Box-Behnken design with experimental values for independent variables.

Run order	Coded level of variables			Actual level of variables			Observed response	Predicted response
	X_1	X_2	X_3	X_1	X_2	X_3	E	E
1	0	1	-1	30	0.25	2	98%	98%
2	-1	0	0	0	0.13	4.5	100%	96%
3	0	-1	-1	30	0.06	2	94%	96%
5	-1	1	0	0	0.25	4.5	100%	101%
6	0	1	1	30	0.25	7	67%	69%
7	1	0	-1	60	0.13	2	87%	101%
8	1	-1	0	60	0.06	4.5	38%	48%
9	0	0	0	30	0.13	4.5	57%	60%
10	0	0	0	30	0.13	4.5	57%	60%
11	-1	0	-1	0	0.13	2	100%	102%
12	0	0	0	30	0.13	4.5	57%	60%
13	0	-1	1	30	0.06	7	67%	72%
14	-1	-1	0	0	0.06	4.5	100%	100%
15	0	0	1	30	0.13	7	63%	67%
16	0	1	0	30	0.25	4.5	57%	64%

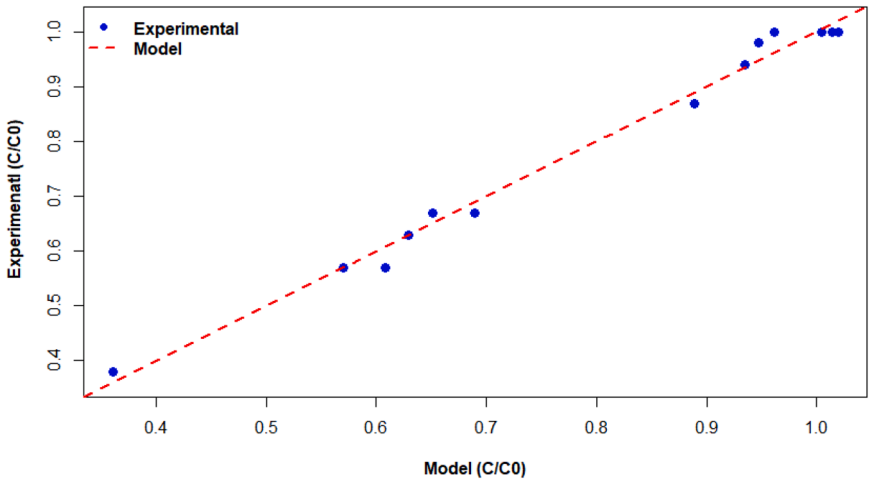


Fig. 11. Correction between predicted and experimental photocatalytic degradation of AG over CZYbEG photocatalyst.

of regression coefficients (Table 4). The model was highly significant ($F = 58.07$, $p = 0.00159$), accounting for most of the variation in GA degradation (Sum of Squares = 0.6391 out of 0.6452). Among the linear terms, irradiation time (X_1) and pH (X_3) exerted significant effects ($p < 0.0001$), whereas catalyst dosage (X_2) was not significant ($p = 0.629$). All quadratic terms were significant ($p < 0.05$), confirming the curvature of the response surface. Regarding interaction terms, only $X_1 \times X_3$ showed a statistically relevant contribution ($p = 0.032$), while those involving X_2 were negligible. The low residual variance (SS = 0.0061) indicated a generally good fit. However, the lack-of-fit test was highly significant ($F \approx 4.18 \times 10^{30}$, $p < 0.00001$), suggesting that despite the strong predictive ability, the current model does not fully capture systematic variability, and the inclusion of additional descriptors may be required to further improve model adequacy.

The interaction effects between the independent variables are illustrated in the 3D response surface plots of Fig. 12. For each diagram, one variable was fixed at its central level while the other two were varied. Fig. 12a shows that increasing both irradiation time (X_1) and catalyst dosage (X_2) enhances GA degradation (lower C/C_0), although the effect of dosage tends to level off beyond 0.125 g L^{-1} . Fig. 12b highlights the strong influence of irradiation time and solution pH (X_3), with maximum efficiency observed around natural pH (≈4.5). Fig. 12c confirms that the combined effect of dosage and pH follows a similar trend, with optimal activity reached at intermediate values.

Overall, the response surfaces indicate the existence of an optimal operational window, beyond which further increases in catalyst loading or extreme pH adjustments do not translate into significant performance gains. These observations are consistent with the ANOVA results, which identified irradiation time and pH as the most significant factors, and with previous response surface studies on photocatalytic systems, further supporting the reliability of the quadratic model.

Table 4
Analysis of variance (ANOVA)for the derived response surface methodology (RSM)model.

Sources	Sum of Squares	Df	Mean Square	F-value	p-value
Model	0.6390597	9	0.071066	58.072	0.00015
X_1	0.262735	1	0.262735	214.8762	< 0.0001*
X_2	0.000323	1	0.000323	0.2639	0.629367
X_3	0.170835	1	0.170835	139.7167	< 0.0001*
X_1^2	0.011698	1	0.011698	9.5673	0.02706
X_2^2	0.011576	1	0.011576	9.4677	0.02756
$X3^2$	0.099389	1	0.099389	81.2847	0.0002803
$X_1 \times X_2$	0.004213	1	0.004213	3.4453	0.1225735
$X_1 \times X_3$	0.077644	1	0.077644	63.50003	0.0005020
$X_2 \times X_3$	0.000647	1		0.5289	0.4996693
Residual	0.0061136	5	0.0012227		
Lack of fit	0.0061136	3	0.0020378		
Pure error	< 0.0001	2	< 0.0001		
Cor total	0.064517	14			

4.7. Possible photocatalytic reaction mechanism driven by the CZYbEG-750 photocatalyst

To elucidate the role of reactive oxygen species (ROS) in GA degradation, scavenger experiments were carried out under optimized conditions (0.125 g L^{-1} catalyst dosage, 5 mg L^{-1} GA initial concentration, spontaneous pH). Disodium ethylenediamine tetra-acetate (EDTA, 10 mmol L^{-1}) was used to quench photogenerated holes (h^+) [67], isopropanol (IPA, 10 mmol L^{-1}) to trap hydroxyl radicals (•OH) [68], and nitrogen (N_2, 142 Ncc min^{-1}) to suppress superoxide radicals ($\bullet O_2^-$) [35].

The effect of scavengers on the photocatalytic activity of CZYbEG-750 was first evaluated in terms of the apparent degradation rate constant (k_{deg}) (Fig. 13). In the absence of scavengers, k_{deg} reached its maximum value (~0.041 min^{-1}). The introduction of isopropanol (IPA) and nitrogen (N_2) significantly reduced the kinetic constant, while the strongest inhibition was observed upon addition of EDTA, where k_{deg} dropped almost to zero. This clearly indicates that photogenerated holes (h^+) are the primary oxidative species in GA degradation, whereas hydroxyl radicals (•OH) and superoxide radicals ($\bullet O_2^-$) also contribute, but to a lesser extent.

The impact of scavengers was also reflected in TOC removal efficiencies. Without scavengers, a mineralization degree of 72.3% was achieved after 180 min. In contrast, TOC removal decreased to 55.4% in the presence of IPA and 57% under N_2 atmosphere, while EDTA completely suppressed mineralization. These results confirm the pivotal role of h^+ in driving not only the initial degradation of GA but also its subsequent mineralization, with •OH and $\bullet O_2^-$ acting as auxiliary reactive species [35,67,68].

To rationalize the experimental observations from the scavenger tests, the electronic band structure of the CZYbEG-750 photocatalyst was analyzed. In particular, the valence band (E_{VB}) and conduction band (E_{CB}) edge potentials at the working pH (4.5) were estimated using Mulliken electronegativity theory. This approach allows the prediction of the relative positions of the band edges with respect to the redox potentials of the main reactive species, thereby providing insight into which charge carriers are thermodynamically capable of generating •OH, $\bullet O_2^-$, and h^+ during photocatalysis. The calculations were performed according to the following equations [35,69,70]:

$$\chi_j = \frac{1}{2} \times \left(E_{EAj} + E_{IEj}\right) \text{ where j} = \text{ions } \left(Ce^{4+},\ Zr^{4+},\ Yb^{3+},\ Er^{3+},\ Gd^{3+},\ O^{2-}\right) \quad (5)$$

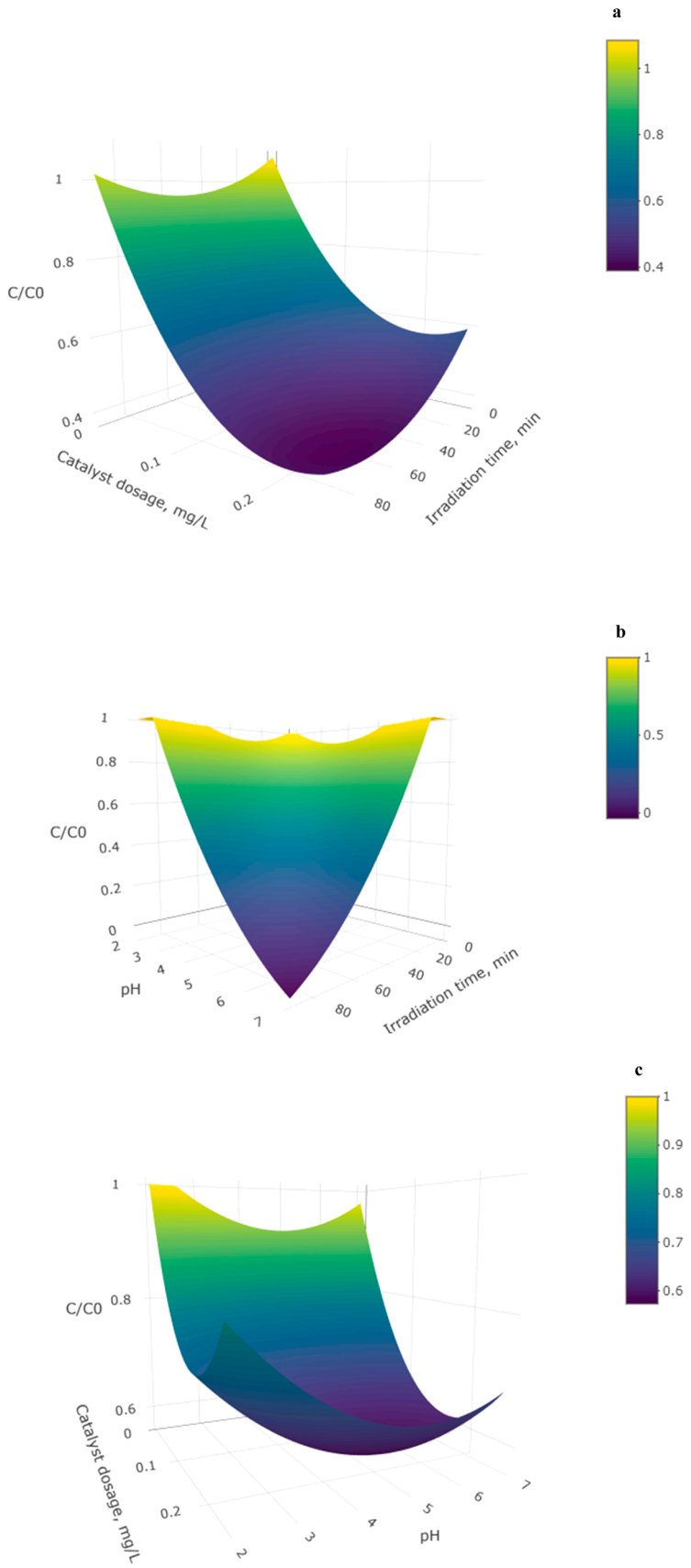


Fig. 12. 3D response surface plots (a,b,c) of interaction between irradiation time (X1), catalyst dosage (X2) and initial pH value (X3) for photocatalytic degradation of GA by CZYbEG-750.

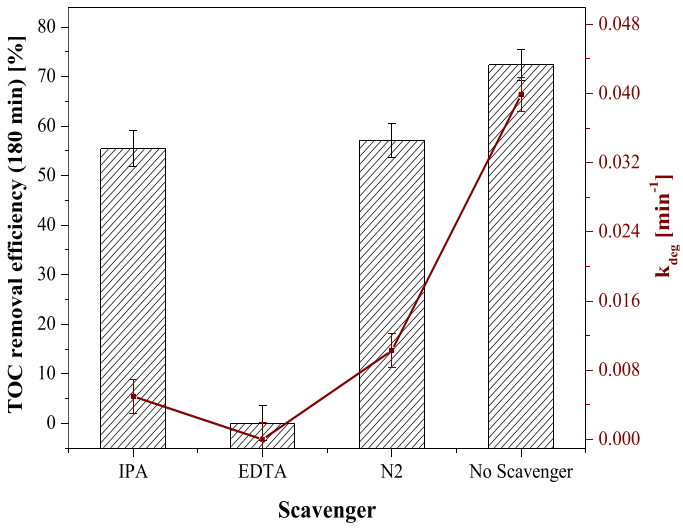


Fig. 13. TOC removal efficiency after 180 min of visible light and k_{deg} values for each scavenger.

$$\chi_{TOT} = (\chi_{Ce}^{a} \times \chi_{Zr}^{b} \times \chi_{Yb}^{c} \times \chi_{Er}^{d} \times \chi_{Gd}^{e} \times \chi_{O}^{f})^{\frac{1}{a+b+c+d+e+f}} \quad (6)$$

$$E_{CB} = \chi - E^{e} - 0.5 \times E_{g} - 0.059 \times pH \quad (7)$$

$$E_{VB} = E_{CB} + E_{g} \quad (8)$$

Where χ_j is the electronegativity of the j species (ions), E_{EAj} is the electron affinity energy of the j species and E_{IEj} is the ionization energy of j species; a, b, c, d, e, f correspond to the atomic fraction of ions; χ_{TOT} is the total electronegativity of CZYbEG-750 (5.44 eV); E_g corresponds to the direct and indirect bandgap of CZYbEG-750 evaluated from the Tauc plot (3.3 and 2.8 eV, respectively, Fig. 5) and E^e is the energy of free electrons on the hydrogen scale (4.5 eV).

In the case of a direct band gap, E_{CB} and E_{VB} potentials were estimated at –1.025 V and + 2.40 V vs. NHE, respectively, whereas for an indirect band gap, the corresponding values were –0.73 V and + 2.08 V vs. NHE. Fig. 14 schematically illustrates the separation of charge carriers and the generation of ROS under both scenarios. Upon visible-light excitation, electrons are promoted from the VB to the CB, leaving behind holes (h^+) that participate in oxidation reactions, while the excited electrons drive reduction processes.

For the direct band gap configuration (Fig. 14a), the E_{VB} (+2.40 V) is sufficiently positive to oxidize GA ($E^{\circ}_{semiquinone/GA}$ = +0.714 V at pH 4.5), making direct hole oxidation thermodynamically favorable compared with •OH generation from water ($E^{\circ}_{\bullet OH/H_2O}$ = +2.46 V vs NHE at pH 4.5) [71]. Meanwhile, the E_{CB} (–1.025 V) lies above the $O_2/\bullet O_2^-$ redox potential (–0.18 V vs NHE [72]), enabling superoxide generation, which can be further reduced to H_2O_2 ($E^{\circ}_{\bullet O_2^-/H_2O_2}$ = +1.057 V vs NHE at pH=4.5), and subsequently converted into •OH radicals ($E^{\circ}_{H_2O_2/\bullet OH}$ = +0.54 V vs NHE at pH 4.5).

Although the direct band gap value (3.3 eV) corresponds to a fundamental transition in the near-UV region, the UV–Vis DRS spectrum of the CZYbEG-750 photocatalyst reveals additional absorption features in the 400–700 nm range (Figure S5 of the Supplementary Material). These features, attributed to intra-4f transitions of rare-earth ions and defect-related states, may introduce intermediate electronic levels within the band structure. Such sub-band-gap states could enable visible-light excitation and contribute to charge carrier generation beyond the fundamental direct transition, thereby providing a plausible explanation for the observed activity under visible irradiation.

A similar trend is observed for the indirect band gap case (Fig. 14b). The indirect band gap (2.8 eV), corresponding to an absorption edge in the visible region, directly supports activation under visible light. Although the E_{VB} (+2.08 V) is less positive, it still allows GA oxidation by h^+, whereas direct •OH generation from water remains thermodynamically unfavorable. The E_{CB} (–0.73 V) remains sufficiently negative to reduce O_2 to $\bullet O_2^-$ and sustain subsequent H_2O_2-mediated pathways.

In this scenario, the combination of indirect band gap excitation and defect-assisted electronic transitions further facilitates visible-light-driven ROS formation.

Overall, the calculated band edge positions confirm that CZYbEG can promote GA degradation through multiple ROS, with h^+ oxidation playing the dominant role and $\bullet O_2^-$/•OH acting as auxiliary contributors. This interpretation is consistent with scavenger experiments (Fig. 13), where EDTA, a selective hole quencher, almost completely suppressed activity [35]. At pH 4.5, gallic acid predominantly occurs in its anionic form [55], which readily interacts with h^+ through oxidative charge transfer. The pronounced inhibition observed in the presence of EDTA corroborates this behavior, highlighting the crucial contribution of holes to the photocatalytic degradation pathway. Based on the experimental evidence obtained from the scavenger tests (Fig. 13) and the calculated band edge positions relative to the redox potentials of the main ROS (Fig. 14), a simplified mechanism is proposed for the photocatalytic degradation of GA over CZYbEG-750.

$$HEO + h\nu \rightarrow h^{+}_{(VB)} + e^{-}_{(CB)}$$

(Reaction 1)

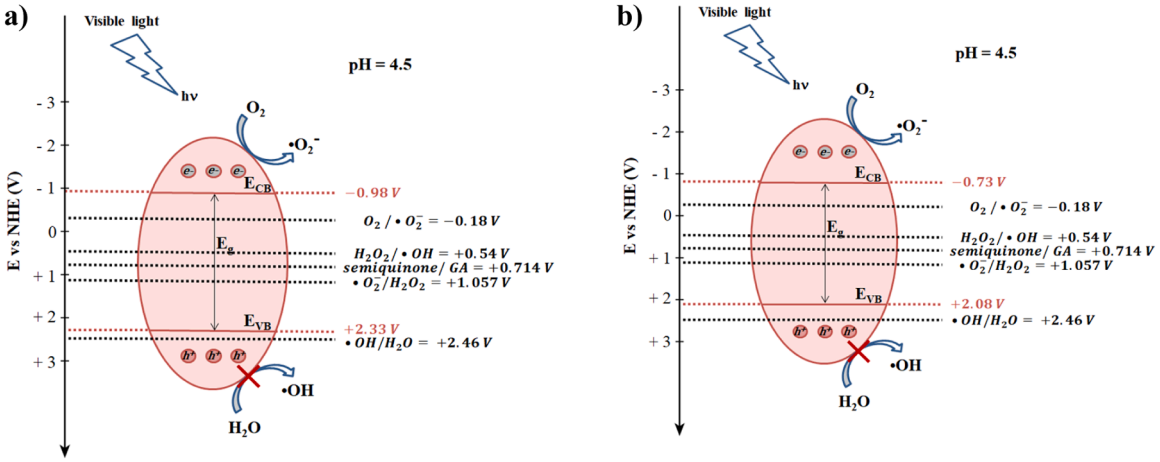


Fig. 14. Schematic diagram of the charge carrier separation and ROS generation in the presence of CZYbEG-750 photocatalyst considered as (a) a direct band gap semiconductor and (b) an indirect band gap semiconductor.

$$C_7H_6O_5 + h^+ \rightarrow \bullet C_7H_5O_5 + H^+$$

(Reaction 2)

$$O_2 + e^- \rightarrow \bullet O_2^-$$

(Reaction 3)

$$\bullet O_2^- + e^- + 2H^+ \rightarrow H_2O_2$$

(Reaction 4)

$$H_2O_2 + e^- + H^+ \rightarrow \bullet OH + H_2O$$

(Reaction 5)

$$\bullet C_7H_5O_5 + \bullet O_2^- / \bullet OH \rightarrow Intermediates \rightarrow H_2O + CO_2$$

(Reaction 6)

Under visible light irradiation, the CZYbEG-750 photocatalyst becomes photoactivated, promoting electrons (e^-) from the VB to the CB and generating photogenerated holes (h^+) in the VB (Reaction 1). These holes oxidize GA to produce semiquinone radicals ($\bullet C_7H_5O_5$) (Reaction 2). Simultaneously, photoexcited electrons reduce dissolved oxygen to superoxide radicals (Reaction 3), which are further reduced to hydrogen peroxide (Reaction 4) and subsequently converted into hydroxyl radicals (Reaction 5). The oxidative degradation of GA is thus driven by the combined action of h^+, $\bullet O_2^-$, and $\bullet OH$ radicals, leading to the formation of intermediates that are progressively mineralized into CO_2 and H_2O (Reaction 6).

Table 5 summarizes the photocatalytic degradation of organic compounds by some recently developed HEOs and other photocatalytic systems, compared to the performance of the CZYbEG-750 photocatalyst.

The electrical energy consumption related to the photodegradation of 90% of the organic pollutant in 1 m^3 of contaminated water was calculated for the photocatalytic systems reported in Table 5, using the Bolton correlation [73,74]:

$$E_{E/O} = \frac{P \times t_{90\%} \times 1000}{V \times 60 \times \ln\left(\frac{c(t_0)}{c(t)}\right)} \quad (9)$$

Where P is the nominal power of the light source (kW), t_{90}% the irradiation time to achieve 90% pollutant removal (min), V the solution volume (L), $c(t_0)$ the initial pollutant concentration (mg L^{-1}), and $c(t)$ the pollutant concentration at the irradiation time corresponding to 90% removal.

The remarkably low energy consumption of ~41.8 kWh m^{-3} observed for CZYbEG-750, compared to values between ~2000 and ~5800 kWh m^{-3} reported for other photocatalysts, clearly demonstrates the superior energy efficiency of the bixbyite HEO.

From a kinetic perspective, the apparent rate constant (k_{app}) of CZYbEG-750 (0.0399 min^{-1}) is considerably higher than those reported for other HEO-based photocatalysts, such as $(CeGdHfPrZr)O_2$ (0.0076 min^{-1}) and $TiO_2/(FeCoGaCrAl)_2O_3$ (0.00547 min^{-1}), and even surpasses some visible-light-driven systems such as $(La_{0.2}Ce_{0.2}Gd_{0.2}Zr_{0.2}Fe_{0.05})O_2$ (0.0171 min^{-1}).

It should also be noted that $BiO[ClBrI(CO_3)_{0.5}]$ exhibited a higher rate constant (0.271 min^{-1}) at the same pollutant concentration (5 mg L^{-1}). However, this result was obtained under a much more intense visible-light source (300 W) and with methyl orange (MO), a dye pollutant that is generally more prone to photocatalytic degradation due to its chromophoric nature. In contrast, CZYbEG-750 successfully achieved the degradation of GA, a non-chromophoric and oxidation-resistant compound, under low-power visible irradiation (10 W). Importantly, despite the lower k_{app}, the energy consumption of CZYbEG-750 (~41.8 kWh m^{-3}) was nearly five times lower than that of $BiO[ClBrI(CO_3)_{0.5}]$ (~192.3 kWh m^{-3}), highlighting the practical advantage of our material in terms of energy efficiency.

Altogether, these results demonstrate that the bixbyite-structured HEO not only exhibits competitive kinetics but also delivers a remarkable reduction in energy demand, underscoring its potential for real-world water treatment applications where both degradation performance and operational costs are critical factors.

Finally, the following Table 6 reports the main photocatalytic performance of different classes of HEOs reported in literature so far, highlighting the lack (to the best of our knowledge) of GA degradation reported under visible light.

4.8. Photocatalytic degradation results on a tap water sample

Photocatalytic tests were finally carried out on a tap water sample spiked with gallic acid (GA), under the optimized conditions (CZYbEG-750 dosage: 0.125 g L^{-1}; C_0: 5 mg L^{-1}; pH: 4.5). The physicochemical composition of the treated tap water is reported in Table S1.

As shown in Fig. 15, both GA degradation (Fig. 15a) and TOC removal (Fig. 15b) efficiencies were slightly lower in tap water than in distilled water, with an average decrease of about 15%. The apparent kinetic constant also decreased significantly when moving from distilled to tap water, reflecting the inhibitory role of dissolved inorganic ions on photocatalytic processes.

The main factor responsible for this reduced activity is the presence of bicarbonate ions (HCO_3^-), which are present at relatively high concentrations in the tap water. Bicarbonates can react with both photogenerated holes and hydroxyl radicals, producing carbonate radical anions ($CO_3\bullet^-$), which are much less reactive and therefore limit GA degradation [85–87].

Additionally, sulfate ions (SO_4^{2-}), even at low concentrations, may further suppress GA degradation by interacting with photogenerated

Table 5
Organic compounds photocatalytic degradation compared with CZYbEG-750 photocatalyst. Acronyms: MB = Methylene Blue, MO = Methyl Orange, OTC = Oxytetracycline, GA = Gallic Acid.

Catalyst	Pollutant	Solution volume (L)	initial concentration (mg L^{-1})	Light source	Degradation time (min)	Rate constant (min^{-1})	Electric energy consumption (kWh m^{-3})	Refs.
$(CeGdHfPrZr)O_2$	MB	0.1	20	UV (100 W)	250	0.0076	2192.97	[70]
$BiO[ClBrI(CO_3)_{0.5}]$	MO	0.096	5	Visible (300 W)	15	0.271	192.26	[75]
$TiO_2/(FeCoGaCrAl)_2O_3$	OTC	0.05	20	UV (32 W)	240	0.00547	1950.04	[31]
$(La_{0.2}Ce_{0.2}Gd_{0.2}Zr_{0.2}Fe_{0.05})O_2$	OTC	0.05	20	Visible (300 W)	180	0.0171	5847.77	[76]
BiOCl microspheres	GA	0.25	20	Solar (12 W)	60	0.00667	119.94	[35]
$(Ce_{0.2}Zr_{0.2}Yb_{0.2}Er_{0.2}Gd_{0.2})_2O_{3+\delta}$	**GA**	**0.1**	**5**	**Visible (10 W)**	**180**	**0.0399**	**41.77**	**Present work**

Table 6
Different HEOs' performances in terms of pollutant degradation.

HEO photocatalyst	Pollutant	Light source	Performance (pollutant degradation)	Ref.
AlCrFeCoNi	Rhodamine B	UV lamp	97.5% in 1 h	[77]
$(CeGdHfPrZr)O_2$	Methylene blue	UV lamp	100% in 4 h	[70]
NbTaZrMoW	Methylene blue	UV lamp	58.77% in 3 h	[29]
$(Mn_{0.6}Cr_{0.6}Co_{0.6}Fe_{0.6}Al_{0.6})O_4$	Methylene blue	UV lamp	100% in 1.5 h	[78]
$(Bi_{0.2}Na_{0.2}Ba_{0.2}K_{0.2}La_{0.2})TiO_3$	Rhodamine B	Xe lamp	98% in 2 h	[79]
$(La_{0.2}Ce_{0.2}Gd_{0.2}Zr_{0.2}Fe_x)O_2$	Tetracycline hydrochloride	Xe lamp	94.5% in 3 h	[76]
$(Ce_{0.2}Pr_{0.2}Zn_{0.2}Nd_{0.2}Tb_{0.2})_2Zr_2O_7$	Congo Red	UV lamp	91.3% in 0.3 h	[80]
$(Ce_{0.2}Pr_{0.2}Zn_{0.2}Nd_{0.2}Tb_{0.2})_2Zr_2O_7$	Methylene blue	UV lamp	79.3% in 0.3 h	[80]
$(La_{0.2}Nd_{0.2}Sm_{0.2}Gd_{0.2}Y_{0.2})_2Zr_2O_7$	Rhodamine B	Hg lamp	90.8% in 2 h	[81]
$(La_{0.2}Nd_{0.2}Sm_{0.2}Gd_{0.2}Y_{0.2})_2Zr_2O_7$	Rhodamine B	UV lamp	70% in 2 h	[82]
$Ce_{0.2}Zr_{0.2}La_{0.2}Pr_{0.2}Y_{0.2}O_2$	Methylene blue	Xe lamp	98.9% in 0.3 h	[28]
$(Co, Mg, Ni, Cu, Zn)_{1-x}Ca_xO$	Methylene blue	Visible light	97% in 1.3 h	[83]
$(Ca_xZrYCeCr)O_2$	Methylene blue	Xe lamp	100% in 1 h	[84]
$(Ce_{0.2}Zr_{0.2}Yb_{0.2}Er_{0.2}Gd_{0.2})_2O_{3+\delta}$	Gallic Acid	Visible light	99.9% in 3 h	This work

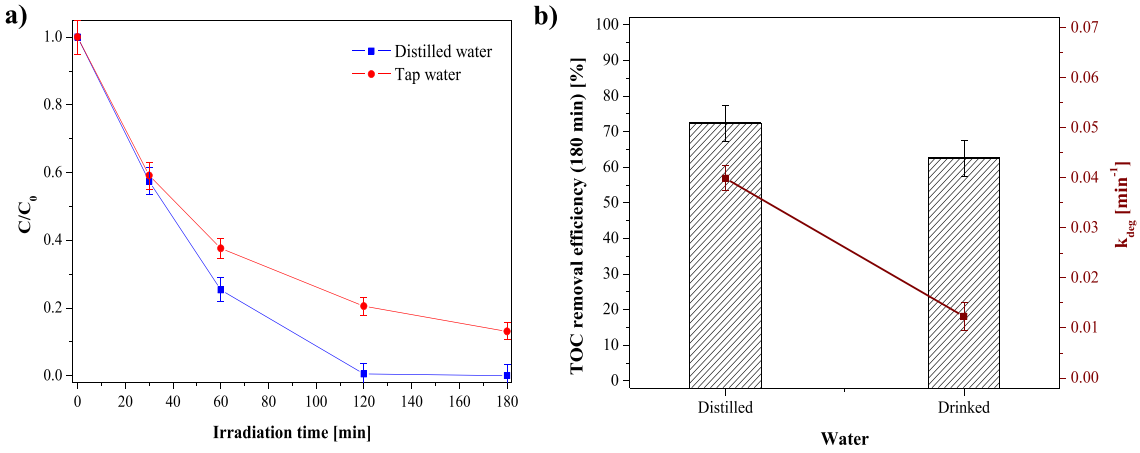


Fig. 15. GA relative concentration as a function of irradiation time; b) TOC removal efficiency (%) after 180 min of visible light carried out in distilled and tap water (labeled as Drinked).

charge carriers [88].

The role of chloride ions (Cl^-) is more complex, as they can convert •OH radicals into reactive chlorine species (Cl•, $Cl_2•^-$, $ClOH•^-$), which may partially inhibit the photocatalytic process, while simultaneously contributing to •OH regeneration, resulting in a compensatory effect [86–88].

Finally, the presence of calcium ions (Ca^{2+}) does not act as a direct scavenger but can promote aggregation of photocatalyst particles, thus reducing the effective surface area and enhancing catalyst deactivation [87,89].

In summary, these results demonstrate that while CZYbEG-750 maintains a high level of photocatalytic activity in real water matrices, the presence of common inorganic ions—especially HCO_3^-—can significantly suppress the degradation kinetics. This emphasizes the importance of testing photocatalysts under realistic conditions to properly evaluate their environmental applicability.

5. Conclusions

In this work, a bixbyite-structured high entropy oxide (HEO), i.e., $(Ce_{0.2}Zr_{0.2}Yb_{0.2}Er_{0.2}Gd_{0.2})_2O_{3+\delta}$ (CZYbEG), was synthesized via a co-precipitation method using ammonia as precipitating agent. Structural characterization highlighted the strong effect of calcination temperature on phase stability and photocatalytic performance. XRD analysis revealed that the sample treated at 750 °C (CZYbEG-750) is a nanocrystalline bixbyite-structured HEO (with a crystallite size lower than 10 nm), while calcination at 1500 °C produced an entropy-stabilized system with increased crystallinity (grain size ≈ 150 nm). Raman spectroscopy, performed on CZYbEG-750, confirmed the presence of defect-related vibrational modes and oxygen vacancies, consistent with its superior photocatalytic efficiency. Moreover, the optical characterization revealed narrow and well-defined absorption features in the 400–700 nm range, attributed to intra-4f electronic transitions of rare-earth ions such as Er^{3+}, Yb^{3+}, and Gd^{3+}. These transitions are expected to introduce intermediate energy levels within the band structure, potentially enhancing visible-light utilization and promoting charge carrier activation under low-power irradiation. Photocatalytic tests demonstrated that CZYbEG-750 efficiently degraded gallic acid (GA), achieving nearly complete degradation (99.9%) and 72.3% mineralization under optimal conditions (0.125 g L^{-1} catalyst dosage, 5 mg L^{-1} GA initial concentration, pH 4.5, 180 min visible light). The effect of pH was found to be critical: the highest efficiency was obtained under spontaneous acidic conditions (pH 4.5), while strongly acidic (pH 2) and alkaline (pH 12) environments drastically reduced photocatalytic activity. This behavior was explained by the interplay between the surface charge of the photocatalyst and the ionization state of GA, which governs pollutant adsorption and the availability of reactive species through electrostatic interactions.

Mechanistic insights, supported by band edge calculations and scavenger tests, indicated that photogenerated holes were the dominant reactive species, with hydroxyl and superoxide radicals contributing synergistically to GA degradation. This analysis identifies the predominant reactive oxygen species but does not aim to elucidate a detailed degradation pathway.

CZYbEG-750 demonstrated good stability and reusability, maintaining high activity after five consecutive cycles.

When tested in real water matrices, the photocatalyst preserved high performance (~85% GA degradation in tap water), although a moderate

reduction in activity was observed compared to distilled water due to the scavenging action of bicarbonates and other inorganic ions, which partially suppress reactive oxygen species formation and reduce the apparent degradation kinetics.

Compared with other photocatalytic systems reported in the literature, CZYbEG-750 exhibited competitive kinetic constants and exceptionally low electrical energy consumption (~40 kWh m^{-3}, versus >2000 kWh m^{-3} for reference systems), highlighting its outstanding energy efficiency.

Although a significant TOC removal was achieved, indicating substantial mineralization, the evaluation of toxicity evolution and the identification of intermediate species are crucial for a complete assessment of environmental impact and will be the focus of future investigations.

In summary, CZYbEG-750 combines single-phase structural stability, defect-rich chemistry, favorable surface area, and visible-light activation, enabling highly efficient degradation of GA. Beyond performance evaluation, this work provides quantitative benchmarks in terms of kinetics and electrical energy consumption, contributing to a more application-oriented assessment of high entropy oxides under visible-light irradiation. Its demonstrated robustness in realistic water matrices, together with its reduced energy demand, further highlights the potential of bixbyite-type high entropy oxides as sustainable photocatalysts for the remediation of persistent organic pollutants.

Author disclosure

During the preparation of this manuscript/study, the authors used ChatGPT 5.2 for the purposes of refining the English Language. The authors have reviewed and edited the output and take full responsibility for the content of this publication.

CRediT authorship contribution statement

Viviana Monfreda: Investigation, Formal analysis. **Andrea Muscatello:** Investigation, Formal analysis. **Olga Sacco:** Writing – original draft, Investigation, Data curation. **Luca Spiridigliozzi:** Writing – review & editing, Methodology, Investigation. **Antonietta Mancuso:** Writing – original draft, Methodology, Investigation, Data curation. **Katia Monzillo:** Investigation, Formal analysis, Data curation. **Serena Esposito:** Writing – original draft, Investigation, Data curation. **Vincenzo Vaiano:** Writing – review & editing, Supervision, Methodology, Conceptualization. **Gianfranco Dell'Agli:** Supervision, Conceptualization.

Declaration of Competing Interest

The authors declare that they have no known competing financial interests or personal relationships that could have appeared to influence the work reported in this paper.

Appendix A. Supporting information

Supplementary data associated with this article can be found in the online version at doi:10.1016/j.cattod.2026.115824

References

[1] A.B.T. Akhtar, S. Naseem, A. Yasar, Z. Naseem, Persistent organic pollutants (POPs): sources, types, impacts, and their remediation. Environmental pollution and remediation, Springer, 2021, pp. 213–246.

[2] S. Sioulas, I. Rapti, C. Kosma, I. Konstantinou, T. Albanis, Photocatalytic degradation of the antidepressant drug Paroxetine using TiO2 P-25 under lab and pilot scales in aqueous substrates, Water Emerg. Contam. anoplastics 4 (2025) (N/A-N/A).

[3] I. Kaul, J.G. Sharma, Nanotechnology for the bioremediation of organic and inorganic compounds in aquatic ecosystem/marine ecosystem, J. Appl. Biol. Biotechnol. 10 (2022) 22–33.

[4] I. Bashir, F.A. Lone, R.A. Bhat, S.A. Mir, Z.A. Dar, S.A. Dar, Concerns and threats of contamination on aquatic ecosystems. Bioremediation and biotechnology: sustainable approaches to pollution degradation, Springer, 2020, pp. 1–26.

[5] A. Mohd, Presence of phenol in wastewater effluent and its removal: an overview, Int. J. Environ. Anal. Chem. 102 (2022) 1362–1384.

[6] K.A.M. Said, A.F. Ismail, Z.A. Karim, M.S. Abdullah, A. Hafeez, A review of technologies for the phenolic compounds recovery and phenol removal from wastewater, Process Saf. Environ. Prot. 151 (2021) 257–289.

[7] W. Raza, J. Lee, N. Raza, Y. Luo, K.-H. Kim, J. Yang, Removal of phenolic compounds from industrial waste water based on membrane-based technologies, J. Ind. Eng. Chem. 71 (2019) 1–18.

[8] B. Badhani, N. Sharma, R. Kakkar, Gallic acid: A versatile antioxidant with promising therapeutic and industrial applications, Rsc Adv. 5 (2015) 27540–27557.

[9] Y. Wu, K. Zhou, S. Dong, W. Yu, H. Zhang, Recovery of gallic acid from gallic acid processing wastewater, Environ. Technol. 36 (2015) 661–666.

[10] H. Nourbakhsh, A. Madadlou, Z. Emam-Djomeh, Y.-C. Wang, S. Gunasekaran, M. E. Mousavi, One-pot procedure for recovery of gallic acid from wastewater and encapsulation within protein particles, J. Agric. Food Chem. 64 (2016) 1575–1582.

[11] B. Boye, E. Brillas, A. Buso, G. Farnia, C. Flox, M. Giomo, G. Sandonà, Electrochemical removal of gallic acid from aqueous solutions, Electrochim. Acta 52 (2006) 256–262.

[12] K.H. Alrman, S. Alhariri, I. Al-Bakri, Evaluation of the Efficiency of a Chitosan Membrane in Removing Gallic Acid from Wastewater Using Adsorption in Batch Mode and Separation by Dead-End Filtration, Jordan J. Chem. (JJC) 18 (2023) 137–149.

[13] T.E. Doll, F.H. Frimmel, Removal of selected persistent organic pollutants by heterogeneous photocatalysis in water, Catal. Today 101 (2005) 195–202.

[14] A.O. Ibhadon, P. Fitzpatrick, Heterogeneous photocatalysis: recent advances and applications, Catalysts 3 (2013) 189–218.

[15] N. Gaur, D. Dutta, A. Singh, R. Dubey, D.V. Kamboj, Recent advances in the elimination of persistent organic pollutants by photocatalysis, Front. Environ. Sci. 10 (2022) 872514.

[16] G. Lama, J. Meijide, A. Sanromán, M. Pazos, Heterogeneous advanced oxidation processes: current approaches for wastewater treatment, Catalysts 12 (2022) 344.

[17] S. Anandan, Y. Ikuma, K. Niwa, An overview of semi-conductor photocatalysis: modification of TiO2 nanomaterials, Solid State Phenom. 162 (2010) 239–260.

[18] T.U. Rahman, H. Roy, A.Z. Shoronika, A. Fariha, M. Hasan, A.K. Alsukaibi, Sustainable toxic dye removal and degradation from wastewater using novel chitosan-modified TiO2 and ZnO nanocomposites, J. Mol. Liq. 388 (2023) 122764.

[19] J. Gaur, S. Kumar, M. Pal, H. Kaur, K.M. Batoo, J.O. Momoh, Current trends: Zinc oxide nanoparticles preparation via chemical and green method for the photocatalytic degradation of various organic dyes, Hybrid. Adv. 5 (2024) 100128.

[20] M. Nemiwal, T.C. Zhang, D. Kumar, Recent progress in g-C3N4, TiO2 and ZnO based photocatalysts for dye degradation: strategies to improve photocatalytic activity, Sci. Total Environ. 767 (2021) 144896.

[21] I. Arora, H. Chawla, A. Chandra, S. Sagadevan, S. Garg, Advances in the strategies for enhancing the photocatalytic activity of TiO2: conversion from UV-light active to visible-light active photocatalyst, Inorg. Chem. Commun. 143 (2022) 109700.

[22] R. Sultana, S.I. Liba, M.A. Rahman, N. Yeachin, I.M. Syed, M.A. Bhuiyan, Enhanced photocatalytic activity in RhB dye degradation by Mn and B co-doped mixed phase TiO2 photocatalyst under visible light irradiation, Surf. Interfaces 42 (2023) 103302.

[23] A.N. Tuama, L.H. Alzubaidi, M.H. Jameel, K.H. Abass, M.Z.H. bin Mayzan, Z. N. Salman, Impact of electron–hole recombination mechanism on the photocatalytic performance of ZnO in water treatment: a review, J. Sol. -Gel Sci. Technol. 110 (2024) 792–806.

[24] C.M. Rost, E. Sachet, T. Borman, A. Moballegh, E.C. Dickey, D. Hou, J.L. Jones, S. Curtarolo, J.-P. Maria, Entropy-stabilized oxides, Nat. Commun. 6 (2015) 8485.

[25] G.M. Tomboc, X. Zhang, S. Choi, D. Kim, L.Y.S. Lee, K. Lee, Stabilization, characterization, and electrochemical applications of high-entropy oxides: critical assessment of crystal phase–properties relationship, Adv. Funct. Mater. 32 (2022) 2205142.

[26] P. Tukur, F. Tukur, Y. Mo, Q. Yan, C. Dun, J. Wei, High entropy oxides: New superior supports for single atom catalysts, Materials 3 (2024) 100192.

[27] Y. Wang, W. Cui, W. Jia, Y. Jiang, H. Zhang, X. Ben, Yang, Entropy-Stabilized Pd/HEO Bifunctional Catalyst for Selective Aqueous-Phase Hydrogenolysis of Cellulose to Ethylene Glycol, EcoEnergy D (2026) e70043.

[28] S. Nundy, D. Tatar, J. Kojčinović, H. Ullah, A. Ghosh, T.K. Mallick, R. Meinusch, B. M. Smarsly, A.A. Tahir, I. Djerdj, Bandgap engineering in novel fluorite-type rare earth high-entropy oxides (RE-HEOs) with computational and experimental validation for photocatalytic water splitting applications, Adv. Sustain. Syst. 6 (2022) 2200067.

[29] O. Zakir, O. Guler, R. Idouhli, A. Nayad, M. Khadiri, S. Guler, A. Abouelfida, B. Dikici, Enhanced photocatalytic abilities of innovative NbTaZrMoW high-entropy alloys (HEAs): a comparative analysis with its high entropy oxide (HEO) counterpart, J. Mater. Sci. 59 (2024) 12050–12064.

[30] Y. Hua, G. Su, Q. Li, J. Pang, B. Sun, Y. Zhang, X. Chen, B. Shi, J. Meng, High entropy oxides as a rising star in pollutant disposal and resource recycling: Emerging advancements and future challenges, Crit. Rev. Environ. Sci. Technol. 55 (2025) 25–48.

[31] J. Dang, W. Pei, X. Hao, Y. Geng, L. Jing, S. Zhao, Y. Dong, X. Chen, J. Hu, Study of the photocatalytic degradation of oxytetracycline using (FeCoGaCrAl) 2O3-doped titanium dioxide as a high-entropy oxide, J. Chem. Technol. & Biotechnol. 100 (2025) 1191–1200.

[32] L. Ming, E. Ghasali, Y. Cheng, C. Zhu, J. Ye, P. Zhang, S. Raza, A. Hayat, Y. Orooji, High entropy oxide (Er2Tm2Yb2Lu2Ho2O15) efficiently and stably degrades Congo red under visible light, Ceram. Int. (2025).
[33] A. Mancuso, K. Monzillo, O. Sacco, L. Spiridigliozzi, V. Monfreda, A. Muscatello, G. Dell'Agli, S. Esposito, V. Vaiano, Engineered synthesis of a novel bixbyite-structured high-entropy oxide (Ce0. 2Zr0. 2Yb0. 2Er0. 2Gd0. 2) 2O3. 4 as a stable and high-performing visible-light-active photocatalyst for multifunctional pollutant degradation, J. Alloy. Compd. 1026 (2025) 180435.
[34] A.L. Luna, M.A. Valenzuela, C. Colbeau-Justin, P. Vázquez, J.L. Rodriguez, J. R. Avendaño, S. Alfaro, S. Tirado, A. Garduño, J.M. De la Rosa, Photocatalytic degradation of gallic acid over CuO–TiO2 composites under UV/Vis LEDs irradiation, Appl. Catal. A Gen. 521 (2016) 140–148.
[35] A.C. Mera, C. Rodríguez, L. Pizarro-Castillo, M. Meléndrez, H. Valdés, Effect of temperature and reaction time during solvothermal synthesis of BiOCl on microspheres formation: implications in the photocatalytic oxidation of gallic acid under simulated solar radiation, J. Sol. -Gel Sci. Technol. 95 (2020) 146–156.
[36] L. Spiridigliozzi, C. Ferone, R. Cioffi, G. Dell'Agli, A simple and effective predictor to design novel fluorite-structured High Entropy Oxides (HEOs), Acta Mater. 202 (2021) 181–189.
[37] L. Spiridigliozzi, C. Ferone, R. Cioffi, G. Dell'Agli, Compositional design of single-phase rare-earth based high-entropy oxides (HEOs) by using the cluster-plus-glue atom model, Ceram. Int. 49 (2023) 7662–7669.
[38] D. Sannino, N. Morante, O. Sacco, A. Mancuso, L. De Guglielmo, G. Di Capua, N. Femia, V. Vaiano, Visible light-driven degradation of Acid Orange 7 by light modulation techniques, Photochem. & Photobiol. Sci. 22 (2023) 185–193.
[39] H. Chaker, N. Ameur, K. Saidi-Bendahou, M. Djennas, S. Fourmentin, Modeling and Box-Behnken design optimization of photocatalytic parameters for efficient removal of dye by lanthanum-doped mesoporous TiO2, J. Environ. Chem. Eng. 9 (2021) 104584.
[40] L. Spiridigliozzi, V. Monfreda, A. Marocco, F. Milano, A. Vendittelli, G. Dell'Agli, Effect of Synthesis and Processing Conditions on the Sintering Behavior and Total Conductivity of High-Entropy Fluorite/Bixbyite Oxides (RE-HEOs), Materials 18 (2025) 2663.
[41] L. Spiridigliozzi, G. Dell'Agli, M. Biesuz, V.M. Sglavo, M. Pansini, Effect of the precipitating agent on the synthesis and sintering behavior of 20 mol% Sm-doped ceria, Adv. Mater. Sci. Eng. 2016 (2016) 6096123.
[42] L. Spiridigliozzi, G. Accardo, E. Audasso, B. Bosio, S.P. Yoon, G. Dell'Agli, Synthesis of easily sinterable ceramic electrolytes based on Bi-doped 8YSZ for IT-SOFC applications, AIMS Mater. Sci. 6 (2019).
[43] D.M.D.M. Prabaharan, K. Sadaiyandi, M. Mahendran, S. Sagadevan, Structural, optical, morphological and dielectric properties of cerium oxide nanoparticles, Mater. Res. 19 (2016) 478–482.
[44] Z. Wu, M. Li, J. Howe, H.M. Meyer Iii, S.H. Overbury, Probing defect sites on CeO2 nanocrystals with well-defined surface planes by Raman spectroscopy and O2 adsorption, Langmuir 26 (2010) 16595–16606.
[45] G. Jayakumar, A. Albert Irudayaraj, A. Dhayal Raj, A comprehensive investigation on the properties of nanostructured cerium oxide, Opt. Quantum Electron. 51 (2019) 312.
[46] O. Elmutasim, A.G. Hussien, A. Sharan, S. AlKhoori, M.A. Vasiliades, I.M.A. Taha, S. Kim, M. Harfouche, A.-H. Emwas, D.H. Anjum, Evolution of oxygen vacancy sites in ceria-based high-entropy oxides and their role in N2 activation, ACS Appl. Mater. & Interfaces 16 (2024) 23038–23053.
[47] W. Zhang, W. Zhang, H. Fei, J. Yan, Z. Li, S. Kang, S. Ren, Z. Wang, H. Shui, A robust ceria-based high entropy oxide catalyst for efficient propane oxidation, Fuel 380 (2025) 133252.
[48] L. Xu, L. Su, H. Wang, H. Gao, P. Guo, M. Niu, K. Peng, L. Zhuang, Z. Dai, High-entropy Sm2B2O7 (B= Ti, Zr, Sn, Hf, Y, Yb, Nb, and Ta) oxides with highly disordered B-site cations for ultralow thermal conductivity, J. Mater. Sci. & Technol. 119 (2022) 182–189.
[49] X. Jin, Y. Huang, F. Peng, W. Zheng, X. Song, C. Jiang, Y. Zeng, Study on the thermal properties of high entropy oxides with highly disordered B-site cations, J. Eur. Ceram. Soc. 44 (2024) 5836–5845.
[50] J. Lowther, Spectroscopic transition probabilities of rare earth ions, J. Phys. C Solid State Phys. 7 (1974) 4393–4402.
[51] D.R. Mullins, The surface chemistry of cerium oxide, Surf. Sci. Rep. 70 (2015) 42–85.
[52] W. Bao, H. Shen, Y. Zhang, C. Qian, G. Zeng, K. Jing, D. Cui, J. Xia, H. Liu, C. Guo, High-entropy oxides for energy storage and conversion, J. Mater. Chem. A 12 (2024) 23179–23201.
[53] S. Das, S. Kumar, S. Sarkar, D. Pradhan, C.S. Tiwary, S. Chowdhury, High entropy spinel oxide nanoparticles for visible light-assisted photocatalytic degradation of binary mixture of antibiotic pollutants in different water matrixes, J. Mater. Chem. A 12 (2024) 16815–16830.
[54] B.S. Oliveira, C.M. de Souza D'Anzicourt, C.M.F. Soares, R.L. de Souza, Á.S. Lima, Liquid-liquid extraction of phenolic compounds in systems based on acetonitrile+ water+ polyvinylpyrrolidone at 298.15 K, Sep. Purif. Technol. 211 (2019) 117–123.
[55] C. Nichita, A.-B.F. Mikhailef, E. Vasile, I. Stamatin, Silver nanoparticles synthesis. bioreduction with gallic acid and extracts from Cyperus rotundus L, Dig. J. Nanomater. Biostructures 15 (2020) 419–433.
[56] A. Hayoune, H. Akkari, V. Vaiano, N. Morante, D. Sannino, F. Madjene, Synthesis and characterisation of novel catalyst Ag-TiO2 loaded on magnetic Algerian halloysite clay (Fe3O4-HKDD3) for the photocatalytic activity of methylene blue dye in an aqueous medium, Int. J. Environ. Anal. Chem. 103 (2023) 7697–7714.
[57] G. Singh, M.K. Ubhi, K. Jeet, C. Singla, M. Kaur, A review on impacting parameters for photocatalytic degradation of organic effluents by ferrites and their nanocomposites, Processes 11 (2023) 1727.
[58] R. Kamalesh, A. Saravanan, Y. Ragini, A. Vickram, A review on optimizing photocatalytic performance for effective removal of emerging pollutants: Approaches and applications, J. Water Process Eng. 69 (2025) 106883.
[59] N. Chakinala, P. Ranjan, A.G. Chakinala, P.R. Gogate, Performance comparison of photocatalysts for degradation of organic pollutants using experimental studies supported with DFT and fundamental characterization, Catal. Commun. 174 (2023) 106589.
[60] X. Zhang, W. Shi, T. Wang, X. Wang, C. Li, W. He, Investigation on the dual roles of pollutants adsorption on the catalyst surface during photocatalytic process, J. Water Process Eng. 63 (2024) 105558.
[61] M. Pirilä, M. Saouabe, S. Ojala, B. Rathnayake, F. Drault, A. Valtanen, M. Huuhtanen, R. Brahmi, R.L. Keiski, Photocatalytic degradation of organic pollutants in wastewater, Top. Catal. 58 (2015) 1085–1099.
[62] A. Samal, K. Pouthika, A. Rajesh, S.M. Roopan, G. Madhumitha, Photocatalytic degradation and kinetic investigations of ZnO-SnO2 heterostructures for treatment of methyl violet using non-conventional approach, Inorg. Chem. Commun. 159 (2024) 111809.
[63] A. Dinesh, K. Radhakrishnan, V. Renuga, R.P. Patil, S. Rajadesingu, S. Suthakaran, L. Guganathan, M. Ayyar, M. Santhamoorthy, L. Gnanasekaran, Visible light photocatalytic degradation of tetracycline using copper ferrite nanoparticles synthesized via Glycine-Assisted combustion method, Results Chem. 13 (2025) 102037.
[64] Y. Liu, C. Ye, L. Chen, J. Fan, C. Liu, L. Xue, J. Sun, W. Zhang, X. Wang, P. Xiong, High entropy-driven role of oxygen vacancies for water oxidation, Adv. Funct. Mater. 34 (2024) 2314820.
[65] X. Yan, Y. Tang, C. Ma, Y. Liu, J. Xu, Deactivation and regeneration of photocatalysts: A review, Desalin. Water Treat. 124 (2018) 160–176.
[66] L. Ren, W. Huo, G. Li, W. Choi, T. An, Photocatalytic mechanisms and photocatalyst deactivation during the degradation of 5-fluorouracil in water, Catal. Today 410 (2023) 45–55.
[67] H. Li, Z. Hu, H. Yu, Photocatalytic degradation of PFOA by hydrangea-like BiOCl with high oxygen vacancies co-mediated under superoxide radicals and holes, J. Environ. Chem. Eng. 11 (2023) 110590.
[68] A. Ahmadian, S. Ahmadi, B. Goharrizi, Roles of reactive species in photocatalysis: effect of scavengers and inorganic ions on dye removal from wastewater, Int. J. Environ. Sci. Technol. 20 (2023) 6433–6448.
[69] D.A. Dryer, M.M. Walczak, PH-dependent redox couple: Illustrating the nernst equation using cyclic voltammetry, J. Chem. Educ. 74 (1997) 1195–1197.
[70] M. Anandkumar, P. Kannan, S. Sudarsan, E. Trofimov, High-entropy oxide (CeGdHfPrZr) O2 nanoparticles as reusable photocatalyst for wastewater remediation, Surf. Interfaces 51 (2024) 104815.
[71] G. Iervolino, C. Falchetta, S. Mottola, I. De Marco, V. Vaiano, Light-assisted hydrogen evolution from gallic acid aqueous solutions using RuO2-ZnO composites prepared via supercritical CO2 assisted micronization route, Fuel 388 (2025) 134480.
[72] W.H. Koppenol, D.M. Stanbury, P.L. Bounds, Electrode potentials of partially reduced oxygen species, from dioxygen to water, Free Radic. Biol. Med. 49 (2010) 317–322.
[73] J.R. Bolton, K.G. Bircher, W. Tumas, C.A. Tolman, Figures-of-merit for the technical development and application of advanced oxidation technologies for both electric-and solar-driven systems (IUPAC Technical Report), Pure Appl. Chem. 73 (2001) 627–637.
[74] N. Morante, V. Folliero, F. Dell'Annunziata, N. Capuano, A. Mancuso, K. Monzillo, M. Galdiero, D. Sannino, G. Franci, Characterization and photocatalytic and antibacterial properties of Ag-and TiOx-based (x= 2, 3) composite nanomaterials under UV irradiation, Materials 17 (2024) 2178.
[75] N. Wen, X. Mu, Y. Zhu, Y. Huang, H. Chen, C. Han, L. Ye, Preparation of novel layered high entropy bismuth-based materials and their photocatalytic degradation mechanism, Langmuir 40 (2024) 9020–9027.
[76] D. Jia, T. Chigan, X. Li, H. Li, P. Yang, Photocatalytic degradation performance for high-entropy oxide (La0. 2Ce0. 2Gd0. 2Zr0. 2Fex) O2 enriched with defects, J. Alloy. Compd. 982 (2024) 173808.
[77] K.C. Sembiring, I.A. Fahrezi, M. Muhdarina, A. Afandi, Complex Concentrated Alloy Catalyst of AlCrFeCoNi for Heterogeneous Degradation of Rhodamine B, Bull. Chem. React. Eng. & Catal. 19 (2024) 134–140.
[78] S. Pradhan, K. Barick, N. Anuraag, V. Mutta, N. Prasad, Development of ferrimagnetic (Mn0. 6Cr0. 6Co0. 6Fe0. 6Al0. 6) O4 high entropy oxide for photo-Fenton degradation of organic dye, Appl. Surf. Sci. 688 (2025) 162343.
[79] H. Fu, S. Li, Y. Lin, X. Wu, T. Lin, C. Zhao, M. Gao, C. Lin, Enhancement of piezo–photocatalytic activity in perovskite (Bi0· 2Na0· 2Ba0· 2K0· 2La0. 2) TiO3 oxides via high entropy induced lattice distortion and energy band reconfiguration, Ceram. Int. 50 (2024) 9159–9168.
[80] M. Anandkumar, S. Sudarsan, V.R. Naganaboina, N.K. Bandari, K.S. Litvinyuk, S. G. Singh, E.A. Trofimov, High-entropy (Ce0. 2Pr0. 2Zn0. 2Nd0. 2Tb0. 2) 2Zr2O7 zirconate pyrochlore: A promising photocatalyst for diverse environmental applications, Nanomaterials 15 (2025) 1668.
[81] M. Du, S. Liu, Y. Ge, Z. Li, T. Wei, X. Yang, J. Dong, Preparation and effect of grain size on the thermal stability, phase transition, mechanical property, and photocatalytic property of pyrochlore (La0. 2Nd0. 2Sm0. 2Gd0. 2Y0. 2) 2Zr2O7 high-entropy oxide, Ceram. Int. 48 (2022) 20667–20674.
[82] S. Liu, M. Du, Y. Ge, Z. Li, G.P. Srivastava, J. Wang, T. Wei, Y. Zou, X. Li, Y. Li, Enhancement of high entropy oxide (La0. 2Nd0. 2Sm0. 2Gd0. 2Y0. 2) 2Zr2O7

mechanical and photocatalytic properties via Eu doping, J. Mater. Sci. 57 (2022) 7863–7876.
[83] A. Gautam, S. Das, M.I. Ahmad, Band gap engineering through calcium addition in (Mg, Co, Ni, Cu, Zn) O high entropy oxide for efficient photocatalysis, Surf. Interfaces 46 (2024) 104054.
[84] S.C. Chang, H.-Y. Chen, P.-H. Chen, J.-T. Lee, J.M. Wu, Piezo-photocatalysts based on a ferroelectric high-entropy oxide, Appl. Catal. B Environ. 324 (2023) 122204.
[85] O.N.E.H. Kaabeche, R. Zouaghi, S. Boukhedoua, S. Bendjabeur, T. Sehili, A comparative study on photocatalytic degradation of pyridinium–based ionic liquid by TiO2 and ZnO in aqueous solution, Int. J. Chem. React. Eng. 17 (2019) 20180253.
[86] X. Gao, Q. Guo, G. Tang, W. Peng, Y. Luo, D. He, Effects of inorganic ions on the photocatalytic degradation of carbamazepine, J. Water Reuse Desalin. 9 (2019) 301–309.
[87] R. Rescigno, F.F. Summa, G. Monaco, P. Iannece, M.C. Hidalgo, O. Sacco, V. Vaiano, V. Venditto, Solar light-driven degradation of thiacloprid by polymer composites based on P-doped TiO2 as photoactive phase: Theoretical and experimental assessment of the reaction mechanism and degradation pathway, J. Environ. Chem. Eng. 13 (2025) 116255.
[88] A. Rawat, S.K. Srivastava, C.S. Tiwary, A.K. Gupta, An LED-driven Hematite/Bi 4 O 5 I 2 nanocomposite as an S-scheme heterojunction photocatalyst for efficient degradation of phenolic compounds in real wastewater, J. Mater. Chem. A 13 (2025) 1271–1286.
[89] S. Sun, H. He, C. Yang, Y. Cheng, Y. Liu, Effects of Ca2+ and fulvic acids on atrazine degradation by nano-TiO2: performances and mechanisms, Sci. Rep. 9 (2019) 8880.